OXFORD

Cerebral Cortex, 2024, **34**, bhae195
https://doi.org/10.1093/cercor/bhae195
Advance access publication date 11 May 2024
Original Article

Exploring intricate connectivity patterns for cognitive functioning and neurological disorders: incorporating frequency-domain NC method into fMRI analysis

Bocheng Wang*, for the Alzheimer's Disease Neuroimaging Initiative†

College of Media Engineering, Communication University of Zhejiang, 998 Xue Yuan Street, Qiantang District, Hangzhou, Zhejiang 310018, China

*Corresponding author: College of Media Engineering, Communication University of Zhejiang, Hangzhou, Zhejiang 310018, China. Email: wangboc@cuz.edu.cn

†Data used in preparation of this article were obtained from the Alzheimer's Disease Neuroimaging Initiative (ADNI) database (adni.loni.usc.edu). As such, the investigators within the ADNI contributed to the design and implementation of ADNI and/or provided data but did not participate in analysis or writing of this report. A complete listing of ADNI investigators can be found at: http://adni.loni.usc.edu/wp-content/uploads/how_to_apply/ADNI_Acknowledgement_List.pdf

This study extends the application of the frequency-domain new causality method to functional magnetic resonance imaging analysis. Strong causality, weak causality, balanced causality, cyclic causality, and transitivity causality were constructed to simulate varying degrees of causal associations among multivariate functional-magnetic-resonance-imaging blood-oxygen-level-dependent signals. Data from 1,252 groups of individuals with different degrees of cognitive impairment were collected. The frequency-domain new causality method was employed to construct directed efficient connectivity networks of the brain, analyze the statistical characteristics of topological variations in brain regions related to cognitive impairment, and utilize these characteristics as features for training a deep learning model. The results demonstrated that the frequency-domain new causality method accurately detected causal associations among simulated signals of different degrees. The deep learning tests also confirmed the superior performance of new causality, surpassing the other three methods in terms of accuracy, precision, and recall rates. Furthermore, consistent significant differences were observed in the brain efficiency networks, where several subregions defined by the multimodal parcellation method of Human Connectome Project simultaneously appeared in the topological statistical results of different patient groups. This suggests a significant association between these fine-grained cortical subregions, driven by multimodal data segmentation, and human cognitive function, making them potential biomarkers for further analysis of Alzheimer's disease.

Key words: time series simulation; frequency-domain NC; deep learning; Alzheimer's disease; efficiency network.

Introduction

Alzheimer's disease (AD) is a pressing issue affecting the elderly population worldwide. It serves as a focal point for research in diverse fields such as neuroscience, brain-like computing, and artificial intelligence. AD is characterized by irreversible structural atrophy and functional decline in the brain, encompassing a range of cognitive impairments from mild cognitive impairment in its early stages to a diagnosis of AD. The disease entails comprehensive degradation of various abilities, including vision, hearing, language organization, comprehension, behavioral planning, and social activities (Hajamohideen et al. 2023; Mulyadi et al. 2023; Zhang, Zhao, et al. 2023b). Given the irreversibility and severe consequences of AD, accurate prediction and early-stage intervention are crucial, necessitating the utilization of scientific technologies such as neuroimaging (Franciotti et al. 2023) and genetics (Stevenson-Hoare et al. 2023). These approaches not only contribute to AD research but also lay the groundwork for a profound understanding of the intricate workings of the brain, which remains the most complex and enigmatic organ to date.

In clinical practice, subjective assessments of patients' cognitive abilities are typically conducted using various psychological assessment scales (Lanctôt et al. 2024), such as the Clinical Dementia Rating (CDR) or the Mini-Mental State Examination (MMSE). With the rapid advancement of neuroimaging technology, researchers are increasingly turning to brain imaging techniques to observe the brain; explore regular changes in brain structure, function, connectivity, and metabolism; and elucidate the pathogenesis of cognitive neurological disorders. For instance, Harrison et al. (2020) conducted a systematic review of 37 studies on AD employing diffusion magnetic resonance imaging data, summarizing the relationships among risk genes, decreased anisotropy, and increased diffusivity in the disease. Similarly, Planche et al. (2022) conducted a longitudinal study using magnetic resonance imaging (MRI) data from hundreds of AD patients, revealing significant volume shrinkage in multiple regions such as the hippocampus, amygdala, temporal lobe, and thalamus. Additionally, Corona-Long et al. (2023) recruited cognitively normal older adults, individuals with subjective cognitive decline (SMC), and mild cognitive impairment patients from the Alzheimer's Disease Research Center (ADRC) database. After MRI scanning, they discovered significant differences in the volume of the insular cortex between cognitively normal older adults and patients with mild cognitive impairment, as well as significant differences in the volume of Brodmann area (BA) 36 between control participants and patients with mild cognitive impairment.

Apart from directly utilizing brain imaging data as the research focus, numerous theoretical approaches employ graph theory

Received: March 27, 2024. **Revised:** April 18, 2024. **Accepted:** April 23, 2024

to construct complex brain network structures that represent the structural connectivity and functional communication characteristics of the brain (Matsui and Yamashita 2023). In this regard, a common approach involves initially partitioning the brain into cortical or subcortical regions and subsequently calculating the correlations or causality between functional magnetic-resonance-imaging (fMRI) blood-oxygen-level-dependent (BOLD) signals in each region to form an $N \times N$ brain connectivity matrix. N represents the level of detail in brain parcellation, encompassing common parcellation schemes such as BAs (Berron et al. 2021), Automated Anatomical Labeling (AAL) (Ahmadi et al. 2022), and the Desikan–Killiany atlas (Sheng et al. 2022). For instance, Hrybouski et al. (2023) investigated changes in functional connectivity within the medial temporal lobe and its immediate functional neighbors in healthy aging individuals, preclinical AD individuals, and individuals with mild cognitive impairment or mild AD. They discovered that the internal connectivity of the anterior and posterior medial temporal lobe networks decreased with age, and as age increased, the decoupling between the anterior and posterior segments of the medial temporal lobe increased. The subregions of the posterior medial temporal lobe, particularly the perirhinal cortex, exhibited greater susceptibility to age-related functional loss compared to their counterparts in the anterior medial temporal lobe. Different parcellation methods significantly differ in terms of the number of brain regions, partitioning criteria, and acceptance, which are closely linked to the quality of the resulting brain connectivity matrix. It is worth noting that in 2017, the Human Connectome Project Multimodal Parcellation (HCP MMP) (Glasser et al. 2016) proposed by the Human Connectome Project team at Washington University offered new possibilities for generating human brain connectivity matrices, enabling researchers to explore the functional connections between human cognitive abilities and a greater number of subregions in high-quality, fine-grained, and multimodal brain parcellations (Schrouff et al. 2018; Jitsuishi and Yamaguchi 2022).

In addition to correlation-based brain connectivity matrices, there is also research (Mohammadian et al. 2023) suggesting the application of causality analysis methods to elucidate the directionality of communication between different brain regions, aiding in a deeper understanding of the cognitive functional mechanisms of the brain. For example, researchers Cao et al. (2024) collected electroencephalogram (EEG) data from three groups consisting of a total of 60 participants, including healthy controls (HCs), AD patients, and Parkinson's disease patients. They employed five causal connectivity assessment methods, including partial directed coherence (PDC), generalized partial directed coherence (GPDC), directed transfer function (DTF), full-frequency direct transfer function (ffDTF), and Geweke–Granger causality (GGC), to construct a 23×23 brain effective network for investigation. However, there is currently no widespread consensus on the comparative performance of various causal relationship theories in brain science data analysis, particularly regarding the application of widely used Granger causality (GC) or GC-like methods from the field of economics in neuroscience. Some studies (Stokes and Purdon 2017; Barnett et al. 2018) have pointed out potential flaws in inferring causal relationships between variables using these methods, raising concerns among researchers. Hu et al. (2011, 2012) proposed a novel causal relationship analysis method, the NC method, which demonstrated its effectiveness in EEG data through theoretical derivation and simulation experiments, comparing it with GC theory. In previous research (Wang et al. 2023), we further extended the NC method to time-domain fMRI data processing and applied it to analyze brain connectivity data in AD patients. Meanwhile, more studies indicate the importance of frequency-domain causal modeling in exploring brain connectivity mechanisms (Xue et al. 2023). Therefore, in this study, we further integrate the novel frequency-domain causal relationship approach into fMRI data analysis to investigate its potential in constructing brain effective networks and revealing variations in brain region connectivity in individuals with different levels of cognitive impairment.

Materials and methods

The research method employed in this study is illustrated in Fig. 1. It consists of two main parts: The upper panel focuses on mathematical modeling of causal relationships at different levels between simulated fMRI data with both bivariate and multivariate settings. The integrated frequency-domain NC method proposed in this study is utilized to detect the causal directionality and assess the consistency of causal inference results with ground truth. It is also compared with three other commonly used frequency-domain causal analysis methods to evaluate their respective performance.

The lower panel describes the analysis of real fMRI data from individuals with varying degrees of cognitive impairment to validate the effectiveness of the integrated frequency-domain NC theory proposed in this study. Additionally, it aims to reveal the variability patterns of causal topological connectivity and centrality among cognitive-related brain regions.

Frequency-domain NC theory

Firstly, the novel frequency-domain causal relationship research method (NC) proposed by Hu et al. (2012) is introduced. To establish a mathematical model that captures the mutual influences among multiple stationary time series with zero mean, we employ a sophisticated joint regression model, as depicted by Equation (1). Specifically, let $\boldsymbol{X_{1,t}}, \boldsymbol{X_{2,t}}, \ldots \boldsymbol{X_{n,t}}$ represent n time series variables. The value of $\boldsymbol{X_1}$ at the current time point is determined by a weighted combination of its own past values and the past values of other variables. The model incorporates $\boldsymbol{\eta_i}$ ($i = 1, 2, \ldots, n$) as the noise term or fitting error. The index j varies from 1 to m, where m represents the lag factor of the time series and can be determined by computing the Akaike information criterion (AIC) or Bayesian information criterion (BIC) values. Notably, $\boldsymbol{a_{\phi \to \rho, j}}$, where φ and ρ are both within the range $[1, n]$, denotes the weight of the influence that the time series φ exerts on the time series ρ within the jth lag term.

$$\begin{cases} X_{1,t} = \sum_{j=1}^{m} a_{1\to 1,j} X_{1,t-j} + \sum_{j=1}^{m} a_{2\to 1,j} X_{2,t-j} + \cdots + \sum_{j=1}^{m} a_{n\to 1,j} X_{n,t-j} + \eta_{1,t} \\ X_{2,t} = \sum_{j=1}^{m} a_{1\to 2,j} X_{1,t-j} + \sum_{j=1}^{m} a_{2\to 2,j} X_{2,t-j} + \cdots + \sum_{j=1}^{m} a_{n\to 2,j} X_{n,t-j} + \eta_{2,t} \\ \quad \cdot \\ \quad \cdot \\ \quad \cdot \\ X_{n,t} = \sum_{j=1}^{m} a_{1\to n,j} X_{1,t-j} + \sum_{j=1}^{m} a_{2\to n,j} X_{2,t-j} + \cdots + \sum_{j=1}^{m} a_{n\to n,j} X_{n,t-j} + \eta_{n,t} \end{cases} \quad (1)$$

In the joint regression model Equation (1), a Fourier transform is applied to both sides to convert the signals from the time domain to the frequency domain for analysis, as shown in Equation (2). In this equation, the frequency of the transformed signal is denoted by f, and the term $\boldsymbol{a_{\phi \to \rho}}(\boldsymbol{f})$ represents the summation of $\boldsymbol{a_{\phi \to \rho, j}}$ multiplied by the complex exponential term $\boldsymbol{e^{-i2\pi fj}}$, where φ and ρ belong to the range $[1, n]$, and i refers to the imaginary unit.

Simultaneously, a novel causal relationship termed "proportionate causality" $\boldsymbol{N_{X_i \to X_k}}(\boldsymbol{f})$ is defined by Hu et al. in Equation (3).

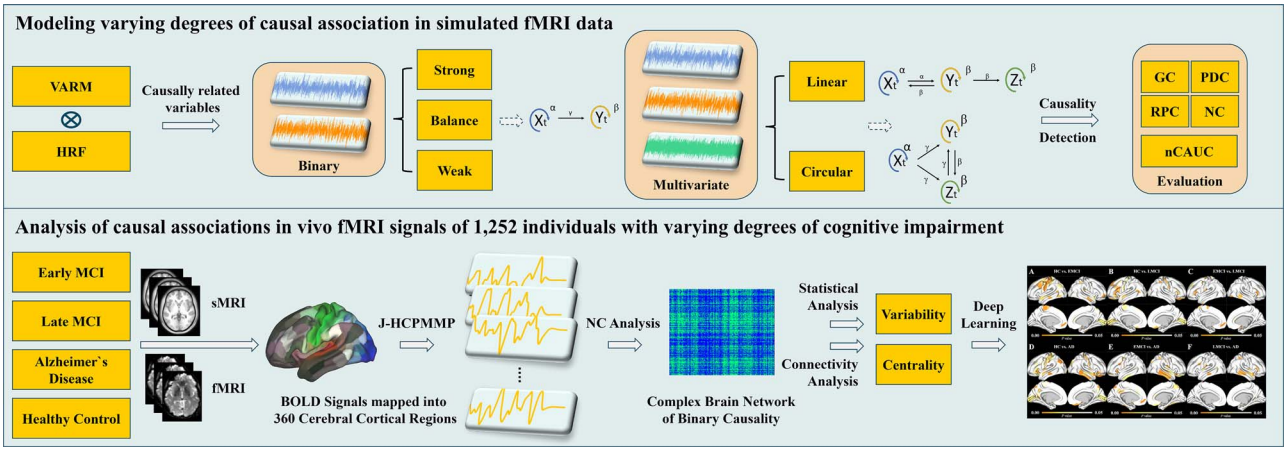

Fig. 1. Research method overview.

It quantifies the proportion of frequency components from time series $\mathbf{X_i}$ that contribute to time series $\mathbf{X_k}$ in the frequency domain. Here, $\sigma^2_{\eta_n(f)}$ represents the variance of the noise term, and $\mathbf{S_{X_iX_i}}(f)$ denotes the spectral density of $\mathbf{X_i}(f)$, where i belongs to the range $[1, n]$.

$$\begin{cases} X_1(f) = a_{1\to1}(f)X_1(f) + a_{2\to1}(f)X_2(f) + \cdots + a_{n\to1}(f)X_n(f) + \eta_1(f) \\ X_2(f) = a_{1\to2}(f)X_1(f) + a_{2\to2}(f)X_2(f) + \cdots + a_{n\to2}(f)X_n(f) + \eta_2(f) \\ \cdots \\ X_n(f) = a_{1\to n}(f)X_1(f) + a_{2\to n}(f)X_2(f) + \cdots + a_{n\to n}(f)X_n(f) + \eta_n(f) \end{cases} \tag{2}$$

$$N_{X_i\to X_k}(f) = \frac{|a_{i\to k}(f)|^2 S_{X_iX_i}(f)}{|a_{1\to k}(f)|^2 S_{X_1X_1}(f) + |a_{2\to k}(f)|^2 S_{X_2X_2}(f) + \cdots + |a_{n\to k}(f)|^2 S_{X_nX_n}(f) + \sigma^2_{\eta_n(f)}} \tag{3}$$

Simulation experiment design

To further investigate the performance of the novel causal relationship in frequency-domain analysis of fMRI data, this study first simulates fMRI BOLD signals and constructs multiple complex multivariate causal relationship models. These models are then combined with four causal analysis methods in the frequency domain: GC, PDC, relative power contribution (RPC), and NC. The aim is to examine whether the causal analysis results obtained by these methods align with the ground truth.

The simulation of the fMRI signals and their causal influences is carried out using the vector autoregression function (VARM) in the MATLAB simulation environment. Based on the modeling scenarios defined by Equations (4–8), time series consisting of 10,000 observations are randomly generated. Following the suggestions by Roebroeck et al. (2005) and consistent with our previous research (Wang et al. 2023), these time series are convolved with a typical hemodynamic response function (canonical hemodynamic response, TR = 100 ms). Subsequently, the signals are down-sampled every TR unit to mimic the process of signal acquisition in fMRI scans. After normalization, Gaussian white noise with a magnitude of 20% is added to simulate fMRI BOLD signals.

Scenario 1: strong causality modeling

Based on Equation (4), a mathematical model for a binary causal relationship is constructed. This model represents a set of relatively strong causal relationships, where the time series X and Y are influenced by their own past values. Simultaneously, the past values of variable X have a weighting factor of 0.1 on the current value of Y. The mathematical relationship between them is depicted in Fig. 2. The purpose of employing weighting factors of 0.9, 0.1, and 0.01 is primarily to delineate varying degrees of causal relationships between variables and to manifest such causality with discernible tendencies. In this scenario, X represents a highly autocorrelated autoregressive model wherein its past values exert an influence of 0.9 times on its current value. Conversely, in joint regression models, Y displays weak autocorrelation at 0.01, while the past values of X exert an influence on the current value of Y exceeding Y's own past values by more than 10-fold. The selection of weighting factors 0.9, 0.1, and 0.01 aims to accentuate these influences, maintaining a magnitude above 10-fold, and further exploration within subsequent methodological comparisons aims to ascertain which approach can more accurately detect such associations.

Fig. 2. Strong causal mathematical model between binary time series.

$$\begin{cases} X_t = 0.9X_{t-1} + \epsilon_1 \\ Y_t = 0.1X_{t-1} + 0.01Y_{t-1} + \epsilon_2 \end{cases} \tag{4}$$

Scenario 2: weak causality modeling

Using Equation (5), a mathematical model for a set of relatively weak binary causal relationships can be constructed. In this model, the time series X is influenced by its own past values with a weighting factor of 0.9. Additionally, X has a smaller influence on the current value of time series Y, with a weighting factor of 0.01. Furthermore, Y is also influenced by its own past values with a weighting factor of 0.1. The specific relationships are illustrated in Fig. 3. It is referred to as weak causal association because the influence of X's past values on Y, originating from X, is reduced by a factor of 10 (from 0.1 to 0.01) compared to the previous simulation, placing greater emphasis on the influence of Y's own past values.

$$\begin{cases} X_t = 0.9X_{t-1} + \epsilon_1 \\ Y_t = 0.01X_{t-1} + 0.1Y_{t-1} + \epsilon_2 \end{cases} \tag{5}$$

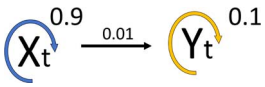

Fig. 3. Weak causal relationships between binary time series.

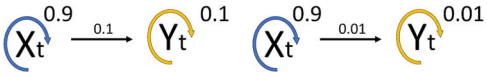

Fig. 4. Balanced causality relationships between binary time series. Left (#1): $\gamma = 0.1$,right (#2): $\gamma = 0.01$.

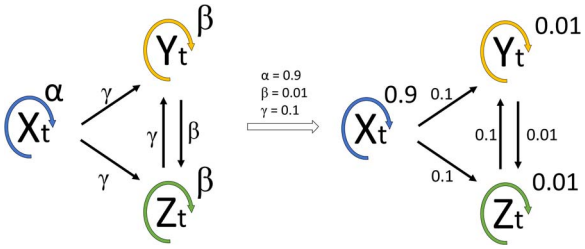

Fig. 5. Simulation of cyclic causal relationships.

Scenario 3: balanced causality modeling

Using Equation (6), a mathematical model is constructed for two additional sets of balanced binary causal relationships. In these relationships, the time series X is influenced by its own past values with a weighting factor of 0.9, and it exerts causal influences on the time series Y with weighting factors of 0.1 or 0.01. Likewise, the time series Y is influenced by its own past values with weighting factors of 0.1 or 0.01, depending on the strength of the influence from X. These relationships are referred to as the "Balanced" scenario in this study. Through these two simulation experiments, the aim is to evaluate the detection performance of different methods in capturing causal influences of varying magnitudes between binary variables, as illustrated in Equation (6) and Fig. 4.

$$\begin{cases} X_t = 0.9X_{t-1} + \epsilon_1 \\ Y_t = \gamma X_{t-1} + \gamma Y_{t-1} + \epsilon_2 \end{cases} \tag{6}$$

Scenario 4: cyclic causality modeling

In this scenario, a cyclic causal model is constructed for a three-element time series, as depicted in Equation (7) and Fig. 5. The time series X, Y, and Z are simulated, with ε representing the error term. X is an autoregressive time series, influenced solely by its own past values with a weighting factor of 0.9. Additionally, X exerts a causal influence on Y and Z with a weighting factor of 0.1 each. Y, in turn, has a causal impact on Z with a weighting factor of 0.01, while Z influences Y with a weighting factor of 0.1 based on its past values. Both Y and Z are influenced by their own past values with a weighting factor of 0.01. Thus, the true causal directions in this simulation are $X_t \to Y_t$, $X_t \to Z_t$, and $Z_t \to Y_t$, with no causal influence from $Z_t \to X_t$.

$$\begin{cases} X_t = 0.9X_{t-1} + \epsilon_1 \\ Y_t = 0.1X_{t-1} + 0.01Y_{t-1} + 0.1Z_{t-1} + \epsilon_2 \\ Z_t = 0.1X_{t-1} + 0.01Y_{t-1} + 0.01Z_{t-1} + \epsilon_3 \end{cases} \tag{7}$$

Scenario 5: transitive causality modeling

In this scenario, a transitive causal model is constructed for a three-element time series, as illustrated in Fig. 6. The time series

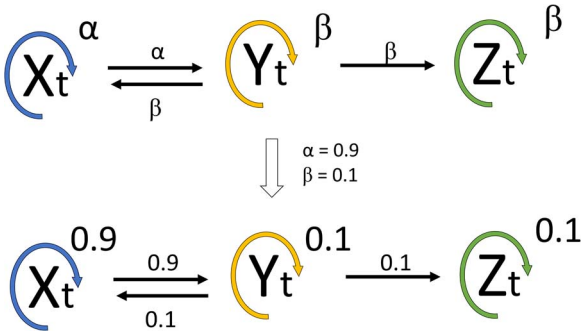

Fig. 6. Simulation of transitive causal relationships.

X, Y, and Z are considered, where X is influenced by its own past values with a weighting factor of 0.9. Additionally, X receives a causal influence of 0.1 from Y. On the other hand, Y influences both X and Z with a weighting factor of 0.1, in addition to being influenced by its own past values. Notably, there is no direct causal effect from X to Z; instead, the causal influence from X to Z is mediated through Y. Thus, the focus of this simulation experiment is to assess the ability of different methods in accurately detecting the indirect causal influence from X to Z.

$$\begin{cases} X_t = 0.9X_{t-1} + 0.1Y_{t-1} + \epsilon_1 \\ Y_t = 0.9X_{t-1} + 0.1Y_{t-1} + \epsilon_2 \\ Z_t = 0.1Y_{t-1} + 0.1Z_{t-1} + \epsilon_3 \end{cases} \tag{8}$$

Simulation evaluation

To compare the magnitudes of different causal effects and reduce the differences caused by varying scales, the study normalizes the causal value curve of $\mathbf{N}_{\mathbf{X_i} \to \mathbf{X_k}}(\boldsymbol{f})$ in Equation (3). The causality measure $Causality_{A \to B}$ or $C_{A \to B}$ is defined as the area under the causal influence curve of variable A on variable B. To accomplish this, the natural logarithm function Z is introduced as defined in Equation (9). When Z is greater than 0, $C_{A \to B} > C_{B \to A}$, and when Z is less than 0, $C_{A \to B} < C_{B \to A}$. If Z is exactly equal to 0, there is no causal influence between variables A and B. The hyperbolic tangent function (tanh) is then applied to Z to obtain the normalized causality area under the curve (nCAUC), as shown in Equation (10). This value maps the causal influence between variables A and B to the range of $[-1, 1]$, avoiding the computational difficulties associated with infinite values in the natural logarithm function. A value of $+1$ indicates that variable A has a significantly greater influence on variable B than vice versa, while a value of -1 indicates that variable B has a significantly greater causal impact on variable A. The normalized nCAUC value is independent of the coordinate axes and only depends on the relative proportions of the causal values, specifically the square difference ratio.

$$Z = \ln \frac{Causality_{A \to B}}{Causality_{B \to A}} = \ln \frac{C_{A \to B}}{C_{B \to A}} \tag{9}$$

$$nCAUC = \tanh(Z) = \frac{e^{Z} - e^{-Z}}{e^{Z} + e^{-Z}} = \frac{e^{\ln \frac{C_{A \to B}}{C_{B \to A} - e} - \ln \frac{C_{A \to B}}{C_{B \to A}}}}{e^{\ln \frac{C_{A \to B}}{C_{B \to A} + e} - \ln \frac{C_{A \to B}}{C_{B \to A}}}} = \frac{\frac{C_{A \to B}}{C_{B \to A}} - \frac{C_{B \to A}}{C_{A \to B}}}{\frac{C_{A \to B}}{C_{B \to A}} + \frac{C_{B \to A}}{C_{A \to B}}} = \frac{{C_{A \to B}}^2 - {C_{B \to A}}^2}{{C_{A \to B}}^2 + {C_{B \to A}}^2} \tag{10}$$

Application in AD study

Table 1 represents the statistical summary of the cognitive impairment patient sample information used in this study. In this study, a total of 1,252 groups of individuals with varying degrees

Table 1. Description of demographic and clinical factors.

	HC	EMCI	LMCI	AD
Total number	575	577	409	266
Male/Female	272/303	321/256	210/199	149/117
Age	72.21 ± 11.61	70.27 ± 8.35	68.97 ± 13.49	73.52 ± 10.97
Education Years	16.13 ± 3.19	16.17 ± 2.89	16.51 ± 3.65	15.57 ± 3.00
CDR	0.04 ± 0.14	0.46 ± 0.19	0.55 ± 0.34	0.89 ± 0.41
MMSE	28.95 ± 1.35	28.15 ± 1.81	26.65 ± 3.41	21.59 ± 3.71
NPI	1.53 ± 4.69	4.11 ± 7.11	5.21 ± 7.67	7.88 ± 9.81
GDS	0.77 ± 1.25	1.92 ± 1.88	1.84 ± 2.05	1.72 ± 1.70
FAQ	0.28 ± 1.36	2.60 ± 4.18	5.18 ± 6.84	14.89 ± 7.70
ADAS	8.68 ± 4.92	12.31 ± 6.70	18.93 ± 10.79	33.01 ± 11.103

CDR, Cognitive Dementia Rating; MMSE, Mini-Mental State Examination; NPI, Neuropsychiatric Inventory; GDS, Geriatric Depression Scale; FAQ, Functional Activities Questionnaire; ADAS, Alzheimer's Disease Assessment Scale.

of cognitive impairment were collected from the Alzheimer's Disease Neuroimaging Initiative (ADNI) dataset in the United States. The sample consisted of 577 groups with early mild cognitive impairment (EMCI), 409 groups with late mild cognitive impairment (LMCI), 266 groups with AD, and 575 groups of HC individuals. The data collection included multimodal magnetic resonance imaging of the head, encompassing structural MRI (sMRI) and resting-state fMRI, as well as equipment magnetic field distribution data (field map).

The sMRI data were acquired using the following parameters: acquisition plane = sagittal; acquisition type = 3D; coil = SENSE-Head-8; field strength = 3.0 tesla; flip angle = 9.0 degrees; matrix X = 256.0 pixels; matrix Y = 256.0 pixels; matrix Z = 170.0; Mfg Model = Intera; pixel spacing X = 1.0 mm; pixel spacing Y = 1.0 mm; pulse sequence = GR; slice thickness = 1.2 mm; TE = 3.2 ms; TI = 0.0 ms; TR = 6.8 ms; weighting = T1.

The fMRI data were acquired with the following parameters: field strength = 3.0 tesla; flip angle = 80.0 degrees; matrix X = 64.0 pixels; matrix Y = 64.0 pixels; Mfg Model = Intera; pixel spacing X = 3.3 mm; pixel spacing Y = 3.3 mm; pulse sequence = GR; slices = 6,720.0; slice thickness = 3.3 mm; TE = 30.0 ms; TR = 3,000.0 ms.

Furthermore, the field map data were acquired with the following parameters: acquisition plane = axial; acquisition type = 3D; coil = SENSE-Head-8; field strength = 3.0 tesla; flip angle = 10.0 degrees; matrix X = 256.0 pixels; matrix Y = 256.0 pixels; matrix Z = 104.0; Mfg Model = Intera; pixel spacing X = 1.0 mm; pixel spacing Y = 1.0 mm; pulse sequence = GR; slice thickness = 3.0 mm; TE = 4.6 ms; TI = 0.0 ms; TR = 20.0 ms; weighting = T2.

Complex brain network modeling

A series of fMRI preprocessing methods was employed to analyze the collected multimodal brain imaging data. The specific steps are as follows. Firstly, the J-HCPMMP method (Sheng et al. 2019) was utilized to register, denoise, and normalize the structural and functional magnetic resonance data from the ADNI dataset. The data was then transformed from native space to the Connectivity Informatics Technology Initiative (CIFTI) space (Glasser et al. 2013; Dickie et al. 2019; Esteban et al. 2019), resulting in 32,492 cortical vertex coordinates for each hemisphere. Based on the HCP MMP brain parcellation method, the cortical surface was divided into 180 brain regions for each hemisphere.

Subsequently, the HCP wb_command tool was employed to input the time series fMRI BOLD signals from the 360 brain regions into the proposed integrated frequency domain NC method. This allowed for the calculation of causal associations between pairs of brain regions, resulting in a directed causal connectivity matrix of size 360 × 360 for each subject, representing the complex brain network. In addition, other widely used frequency-domain causality analysis algorithms such as GC, PDC, and RPC were employed for comparative analysis. Finally, utilizing the Brain Connectivity Toolbox (BCT) (Rubinov and Sporns 2010), various network metrics were computed to evaluate the connectivity and centrality of the directed complex brain network.

Statistical significance analysis

To further analyze and compare the patterns of significant changes in different patient groups, this study conducted a significance analysis on the BCT topological measures calculated in the previous section. Since the distribution characteristics of the samples were not known, a nonparametric statistical test, the Kruskal–Wallis's (KW) test (van der Haar et al. 2023), was employed. Firstly, the KW test was performed on the BCT measures of the 360 brain regions for the four patient groups. This analysis identified brain regions with statistically significant P-values below the 0.05 significance level. Post hoc analysis was then conducted to determine which brain regions exhibited significant differences in the variation of directed causal topologies among different groups. By utilizing the Kruskal–Wallis's test and post hoc analysis, this study aimed to identify brain regions where the directed causal network topologies exhibited significant differences across the different patient groups.

Deep learning and evaluation

In addition to traditional statistical tests for variability, the study incorporated deep learning methods. The integration of deep learning alongside traditional statistical analyses aims primarily to assess the discriminative capacity of various frequency-domain causal analysis methods in processing functional brain imaging data from AD patients. Specifically, this study highlights the superiority of the NC method from both simulated and practical perspectives. Throughout the AD patient identification process, comparisons were conducted among different frequency-domain causal analysis methods to extract topological features of brain connectivity networks. Subsequently, these features were employed to train neural network models, leveraging the classification outcomes of the models to determine which frequency-domain causal analysis method could more accurately extract effective features. The use of deep learning as a validation tool provides a more intuitive assessment of the applicability of frequency-domain NC methods in analyzing functional brain connectivity in AD. While statistical analysis methods often rely on descriptors such as mean, variance, coefficient of variation, or distribution characteristics to depict the variability of patient

Table 2. nCAUC detection results of binary time series causal relationships (for Scenarios 1–3).

Scenario	Time domain		Frequency domain			
	GC	NC	GC	PDC	RPC	Proposed
Strong	0.66	0.99	−1	0.46	−0.99	0.99
Weak	−0.07	0.99	−1	0.23	−1	0.11
Balanced #1	0.01	0.99	−1	0.33	−0.99	0.90
Balanced #2	0.63	0.99	−1	0.59	−0.99	0.28

brain efficiency networks, deep learning classification results serve as a complementary approach to further elucidate the relative merits of different frequency-domain causal methods using intuitive metrics such as accuracy, precision, and recall.

The directed causal network topological connectivity measures of all brain regions were used as the input features for the deep learning's first layer. To ensure the model's robustness and interpretability, a relatively simple deep learning network architecture was chosen. The initial layer consisted of 360 nodes, representing the topological measures derived from the 360 brain regions. A normalization layer was implemented to address dimensional discrepancies between nodes, samples, or groups. The network comprised 16 layers with rectified linear unit (ReLU) activation functions, each composed of 1024 nodes. To prevent overfitting, a dropout layer with a dropout rate ranging from 20% to 50% was inserted prior to the output layer.

Regarding data preparation, the training and testing sets were split in a ratio of 0.8:0.2, and the dataset was randomly partitioned for each iteration using the sklearn tool. The optimization process employed the Adam algorithm with an initial learning rate of 0.00001, a batch size of 16, and a maximum epoch step of 800. The deep learning model was developed using the Keras framework, and the computations were performed on an NVIDIA GeForce RTX 4080 GPU.

To evaluate the model's performance, the study primarily utilized widely accepted evaluation metrics based on the confusion matrix, including accuracy, sensitivity, and recall, among others. These metrics provided insights into the classification performance of the model.

Results

Table 2 presents the results of nCAUC analysis for scenarios 1–3. In scenario 1 (Strong), both the GC and NC methods in the time domain successfully detect the causal influence of X_t on Y_t. However, in the frequency domain, the GC and RPC methods yield incorrect results. The PDC method and the integrated NC theory proposed in this study provide accurate causal directions in fMRI data analysis. Figure 7 illustrates the nCAUC causal analysis curve for scenario 1. In this figure, the red curves in all subplots represent the results that align with the simulation model truth, which corresponds to the true causal direction $X_t \rightarrow Y_t$. The results observed in Fig. 7 are consistent with those presented in Table 2.

For scenario 2 (Weak), in the time domain calculations, the GC method yields negative values, suggesting that the causal influence of Y_t on X_t is greater than that of X_t on Y_t. This contradicts the mathematical definition in this simulation. However, the NC method accurately detects the correct causal direction. In the frequency domain calculations, the GC and RPC methods produce incorrect conclusions, while the PDC method and the proposed method in this study yield correct results. Although the proposed method may exhibit lower sensitivity compared to PDC in numerical terms, it reveals a limitation that it can only qualitatively detect the causal direction and cannot provide quantitative analysis. Figure 8 illustrates the nCAUC causal analysis curve for scenario 2. In this figure, the red curves in all subplots align with the simulation truth, indicating the true causal direction $X_t \rightarrow Y_t$.

For scenario 3 (balanced #1, #2), in the time domain, both the GC and NC methods can detect the correct causal direction. However, in the frequency domain, the GC and RPC methods yield incorrect conclusions. Similarly, the PDC method and the proposed method in this study accurately detect the true causal direction $X_t \rightarrow Y_t$. Figures 9 and 10 depict the nCAUC causal analysis curves for scenario 3. In these figures, the red curves in all subplots align with the simulation truth, indicating the true causal direction $X_t \rightarrow Y_t$. These results are consistent with the calculations presented in Table 2 (scenario: balanced).

Table 3 displays the nCAUC causal analysis results for scenario 4. According to the modeling Equation (7), the true causal directions are determined to be $X_t \rightarrow Y_t$, $X_t \rightarrow Z_t$, and $Z_t \rightarrow Y_t$. In the time domain calculations, it is observed that both the GC and NC methods provide similar and accurate conclusions. Notably, the integrated NC method demonstrates the highest value of 1, emphasizing its effectiveness. However, in the frequency domain calculations, while the PDC method accurately identifies the causal directions $X_t \rightarrow Y_t$ and $X_t \rightarrow Z_t$, it fails to correctly determine the causal direction $Y_t \rightarrow Z_t$. Conversely, both the RPC and GC methods exhibit fundamental errors in discerning the causal relationships in the $X_t \rightarrow Y_t$ and $X_t \rightarrow Z_t$ pairs. On the other hand, the NC method in the frequency domain yields correct conclusions, aligning with the simulation model. Figure 11 illustrates the nCAUC causal analysis curves for scenario 4. The red curves in all subplots are in agreement with the simulation truth, indicating the true causal directions $X_t \rightarrow Y_t$, $X_t \rightarrow Z_t$, and $Y_t \rightarrow Z_t$. The results of the analysis are consistent with those presented in Table 3.

Table 4 presents the nCAUC causal analysis results for scenario 5. In the time domain calculations, both the GC and NC methods accurately detect the three sets of causal influence directions: $X_t \rightarrow Y_t$, $X_t \rightarrow Z_t$, and $Y_t \rightarrow Z_t$. However, in the frequency domain, the RPC method and GC method yield results that contradict the simulation truth, particularly the GC method, which completely misidentifies the causal directions. On the other hand, the PDC method and the proposed method in this study provide correct conclusions. Figure 12 illustrates the nCAUC causal analysis curves for scenario 5. The red curves in all subplots align with the simulation truth, indicating the true causal directions $X_t \rightarrow Y_t$, $X_t \rightarrow Z_t$, and $Y_t \rightarrow Z_t$. These results are consistent with the calculations presented in Table 4.

Fig. 13 shows the performance of the four frequency-domain causal analysis methods when their computed interregional

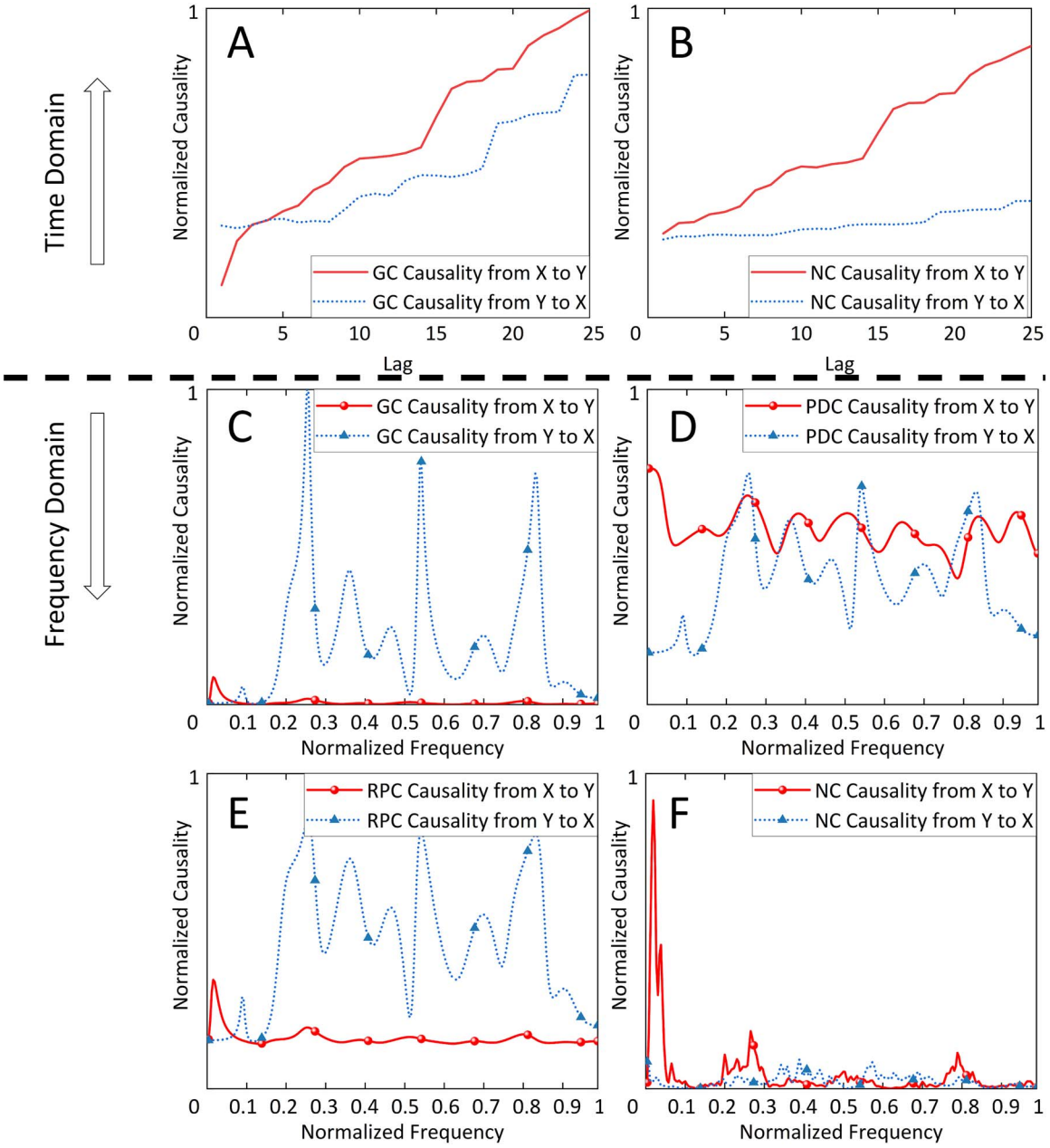

Fig. 7. Strong causal detection results for binary time series. Subplots A and B depict the detection results in the time domain using the GC and NC methods, respectively. The X-axis represents the lag factor. Subplots C–F correspond to the detection results in the frequency domain using the GC, PDC, RPC, and the proposed causal calculation method in this study. The X-axis represents the normalized frequency spectrum.

Table 3. nCAUC causal analysis results for multivariate time series (corresponding to scenario 4, cyclic causality).

	Method	$X_t \to Y_t$	$X_t \to Z_t$	$Y_t \to Z_t$
Time domain	GC	0.75	0.93	−0.23
	NC	1.00	1.00	−0.60
Frequency domain	PDC	0.23	0.33	0.04
	RPC	−1.00	−1.00	−1.00
	GC	−1.00	−1.00	−1.00
	Proposed	1.00	1.00	−0.69

causal values are fed into a deep learning model. From top to bottom, the figure corresponds to GC, PDC, RPC, and the proposed method in this study. On the left side, the model training curves are displayed, with the y-axis representing training accuracy. On the right side, the curves represent the variation of model error, with the y-axis indicating the loss computed using the binary cross-entropy loss function from the Keras development framework.

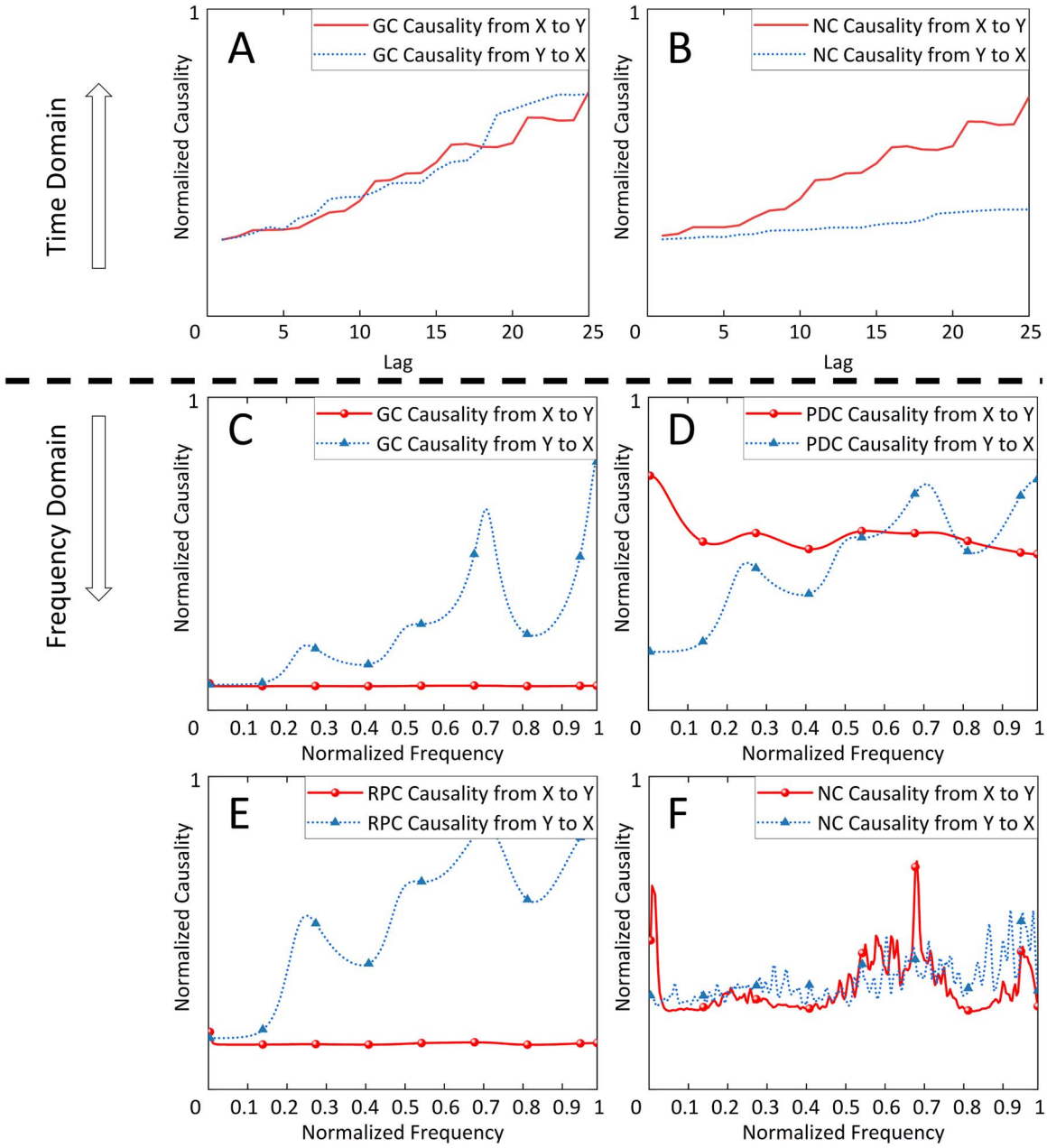

Fig. 8. Weak causal detection results for binary time series.

Table 4. nCAUC causal analysis results for multivariate time series (corresponding to scenario 5, transitive causality).

	Method	$X_t \to Y_t$	$X_t \to Z_t$	$Y_t \to Z_t$
Time domain	GC	0.36	1.00	1.00
	NC	1.00	1.00	1.00
Frequency domain	PDC	0.14	0.94	0.90
	RPC	−0.80	1.00	−0.94
	GC	−1.00	−0.81	−0.94
	Proposed	0.44	1.00	1.00

From the figure, it can be observed that the proposed causal analysis method exhibits slower convergence in the model, reaching its peak around 300–400 epochs (HC vs. LMCI group, represented by the red curve). On the other hand, the other three causal analysis methods achieve their highest training accuracy, close to 100%, at around 100 epochs in different binary classification groups. However, it is still necessary to determine the true performance of the model by evaluating its accuracy on a separate test dataset.

Table 5 and Fig. 14 present the testing performance. In the six groups of binary classification, this study computed three evaluation metrics: accuracy, precision, and recall. In terms of

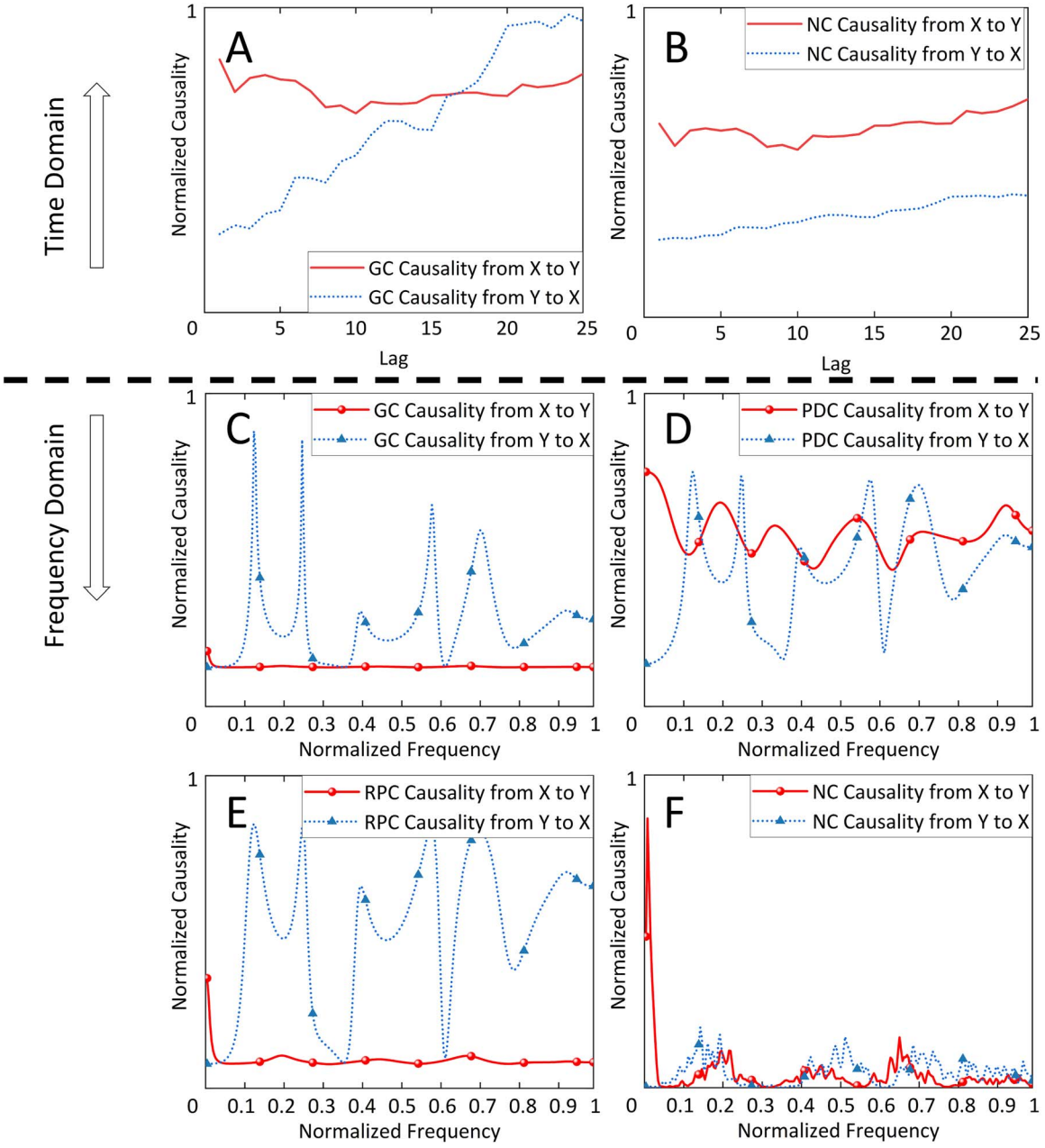

Fig. 9. Causal detection results for binary time series (balanced #1, $\gamma = 0.1$).

classification accuracy, the proposed method in this study demonstrates the best performance among all binary classification scenarios. The highest accuracy score is achieved in the HC vs. AD group, with an accuracy of 0.817. This is followed by the EMCI vs. AD group with 0.763, HC vs. LMCI group with 0.726, EMCI vs. LMCI group with 0.720, LMCI vs. AD group with 0.719, and HC vs. EMCI group with 0.697. The other three methods yield subpar performance in the classification models, significantly lower than the proposed method in this study. Regarding precision and recall, the proposed method also achieves the highest values in the majority of cases. The only exception is in the HC vs. LMCI group, where the precision for the PDC method is 0.719 compared to 0.710 for the proposed method, and the recall for the PDC method is 0.656 compared to 0.627 for the proposed method. In the EMCI vs. LMCI group, the precision for the PDC method is 0.808, while the proposed method achieves a precision of 0.800. Overall, the proposed method demonstrates outstanding performance in most scenarios.

To further compare and analyze the testing performance, this study presents the confusion matrix in Fig. 15. The matrix specifically highlights the model's performance on each individual classification. For instance, in the bottom-right corner of the matrix, corresponding to the proposed method in this study, the labels A–F represent the six binary classification results: HC vs. EMCI, HC vs. LMCI, HC vs. AD, EMCI vs. LMCI, EMCI vs. AD, and LMCI vs. AD. Taking label A as an example, in the actual dataset, there are a total of 120 samples of HC and 111 samples of individuals with EMCI. The numbers on the green diagonal represent the cases where the model's predictions match the actual values. In this case, out of the 120 samples of HC, the model correctly identifies 78 samples as healthy (0.65), while out of the 111 samples of EMCI, the model correctly identifies 83 samples (0.74). Therefore,

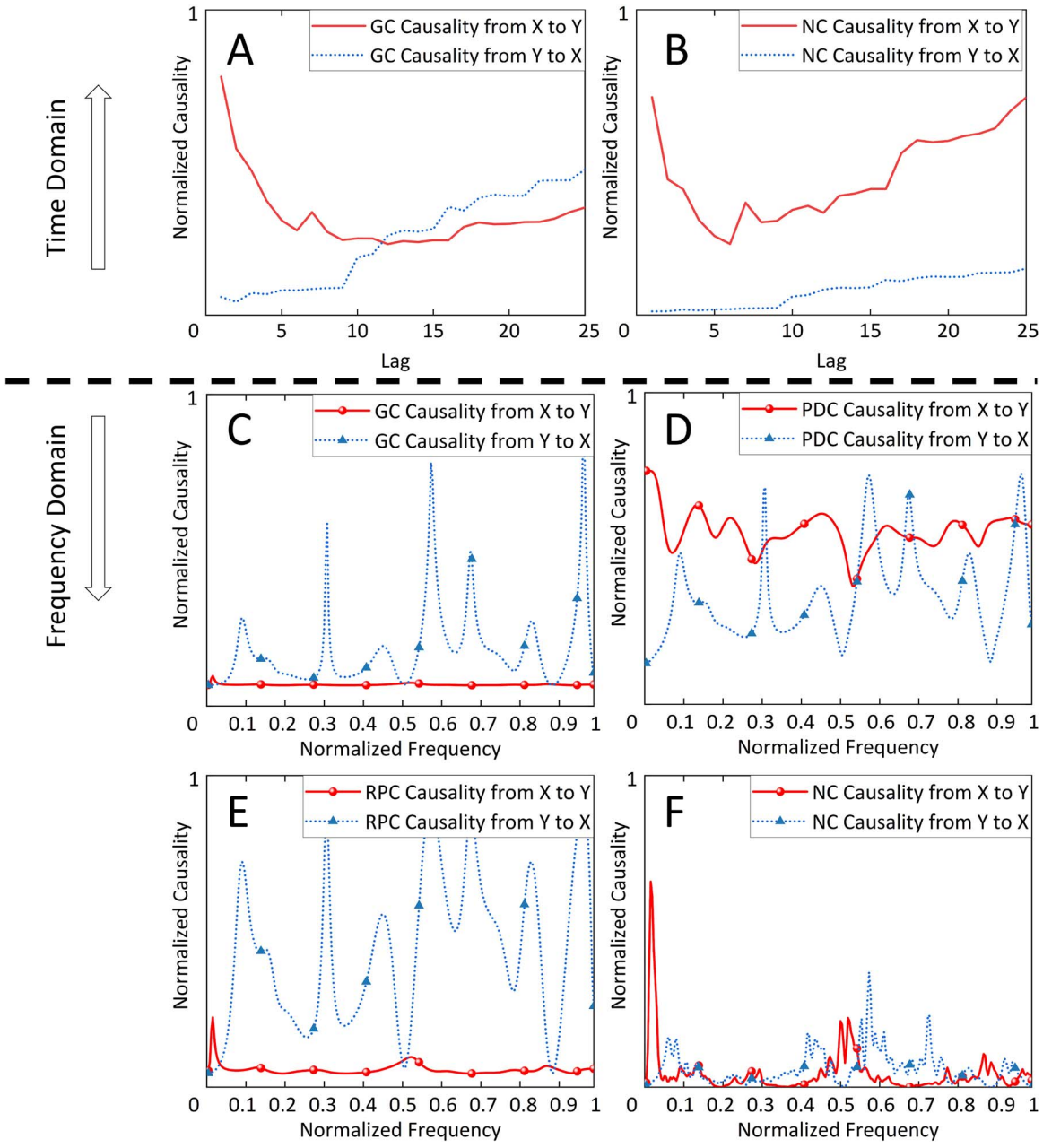

Fig. 10. Causal detection results for binary time series (balanced #2, $\gamma = 0.01$).

Table 5. Model testing performance.

		HC vs. EMCI	HC vs. LMCI	HC vs. AD	EMCI vs. LMCI	EMCI vs. AD	LMCI vs. AD
Accuracy	GC	0.498	0.548	0.651	0.556	0.716	0.659
	PDC	0.649	0.726	0.751	0.662	0.751	0.667
	RPC	0.554	0.604	0.651	0.596	0.639	0.556
	Proposed	0.697	0.726	0.817	0.720	0.763	0.719
Precision	GC	0.474	0.493	0.717	0.375	0.734	0.659
	PDC	0.714	0.719	0.817	0.554	0.808	0.677
	RPC	0.468	0.539	0.701	0.547	0.697	0.588
	Proposed	0.736	0.710	0.822	0.707	0.800	0.745
Recall	GC	0.500	0.398	0.798	0.333	0.903	0.831
	PDC	0.620	0.656	0.831	0.485	0.836	0.823
	RPC	0.531	0.409	0.826	0.407	0.825	0.740
	Proposed	0.650	0.627	0.950	0.616	0.869	0.833

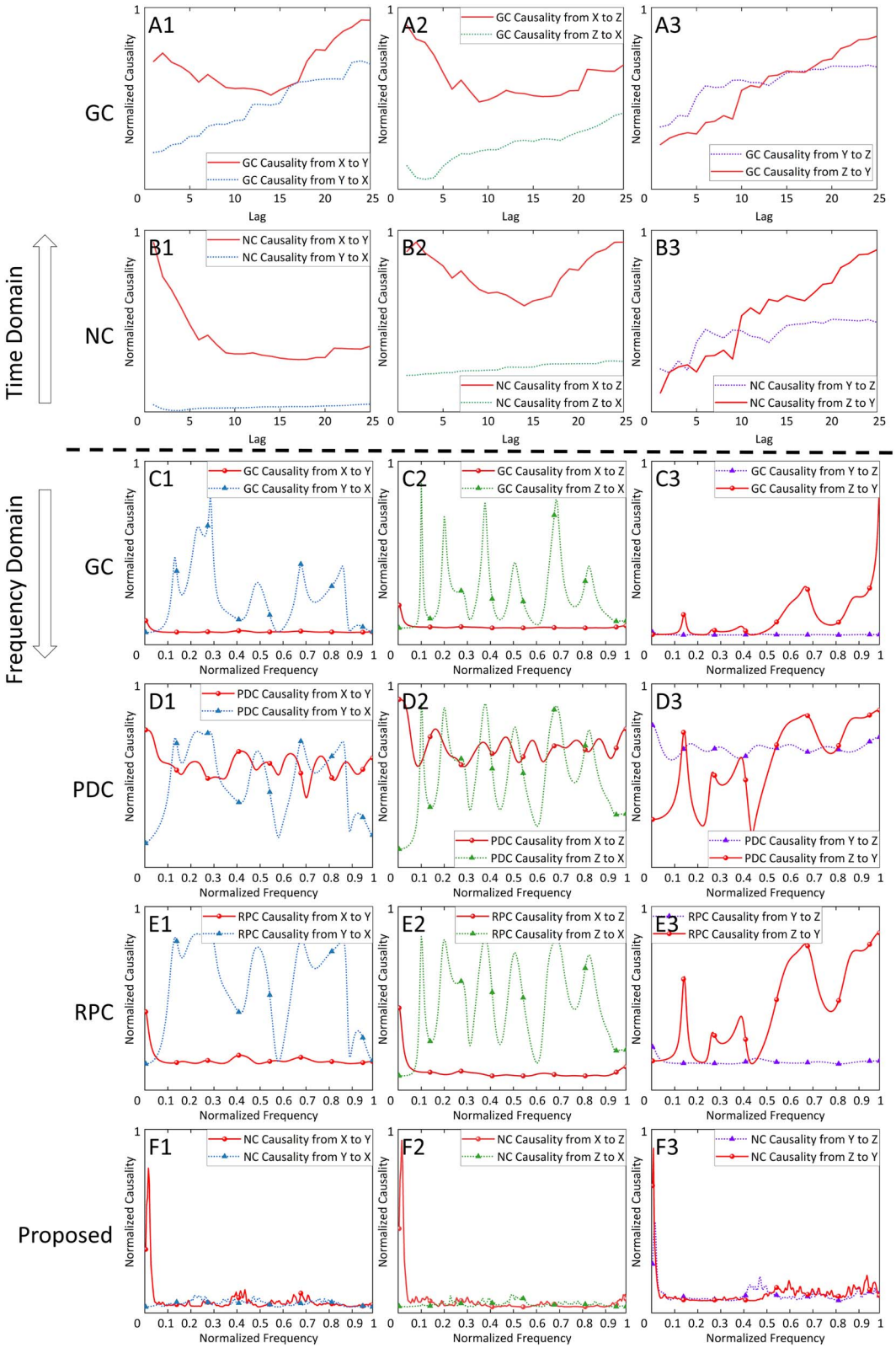

Fig. 11. Simulation of cyclic causal relationships in multivariate causality (corresponding to scenario 4, cyclic causality).

the average classification accuracy for the HC vs. EMCI group is 0.69.

Based on previous research (Wang et al. 2022), the Page Rank Centrality (PC) measure has demonstrated outstanding performance in classification tasks. In this study, it was also computed and analyzed. The KW nonparametric test revealed significant differences among the classification groups in a total of 63 subregions in the left cerebral cortex and 52 subregions in the right cerebral cortex. Further analysis was conducted using post hoc tests, and the detailed statistical findings are presented in Tables 6-11.

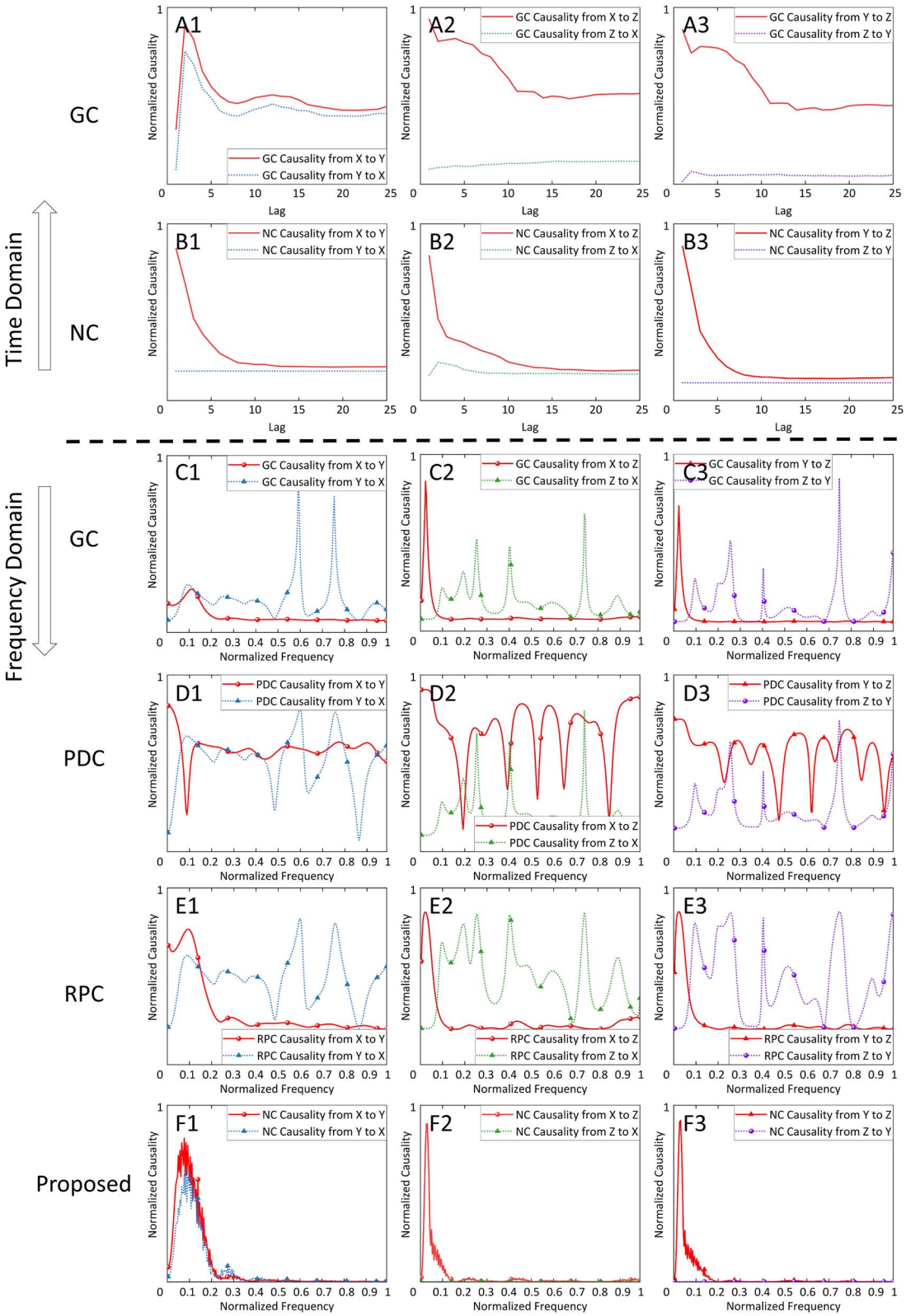

Fig. 12. Simulation of transitive causal relationships in multivariate causality (corresponding to scenario 5, transitive causality).

Table 6 provides the results of the significance difference tests for PC values between the HC and EMCI groups. Among the left cerebral cortex regions, 25 brain regions, and among the right cerebral cortex regions, 21 brain regions exhibited *P*-values below the significance level of 0.05. Notably, four brain regions, specifically the 3a, PEF, V4t, and STGa regions defined by the HCP MMP, displayed significant differences in both the left and right cerebral cortex between the EMCI and HC groups.

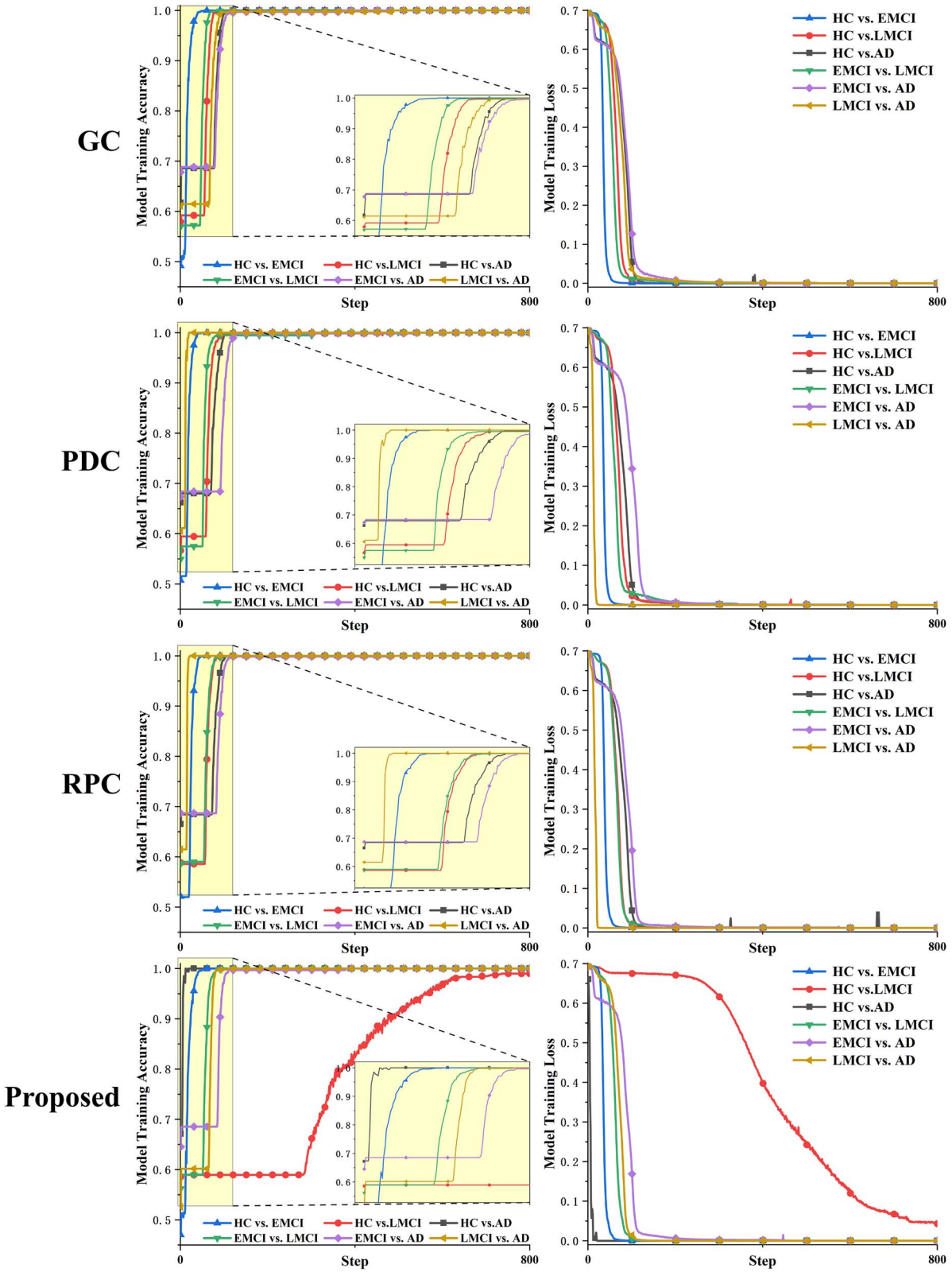

Fig. 13. Training curves (left) and error variation (right) for four frequency domain causal analysis methods.

Table 7 presents the results of the significance difference tests for PC values between the LMCI group and the HC group. In the left cerebral cortex, 21 brain regions, and in the right cerebral cortex, 10 brain regions exhibited *P*-values below the significance level of 0.05. Notably, five brain regions, namely, the OFC (orbitofrontal cortex), V3B, 3a, V1, and 45 regions defined by the HCP MMP, showed significant differences in both the left and right cerebral cortex between the LMCI and HC groups.

Table 8 presents the results of the significance difference tests for PC values between the AD group and the HC group. In the left

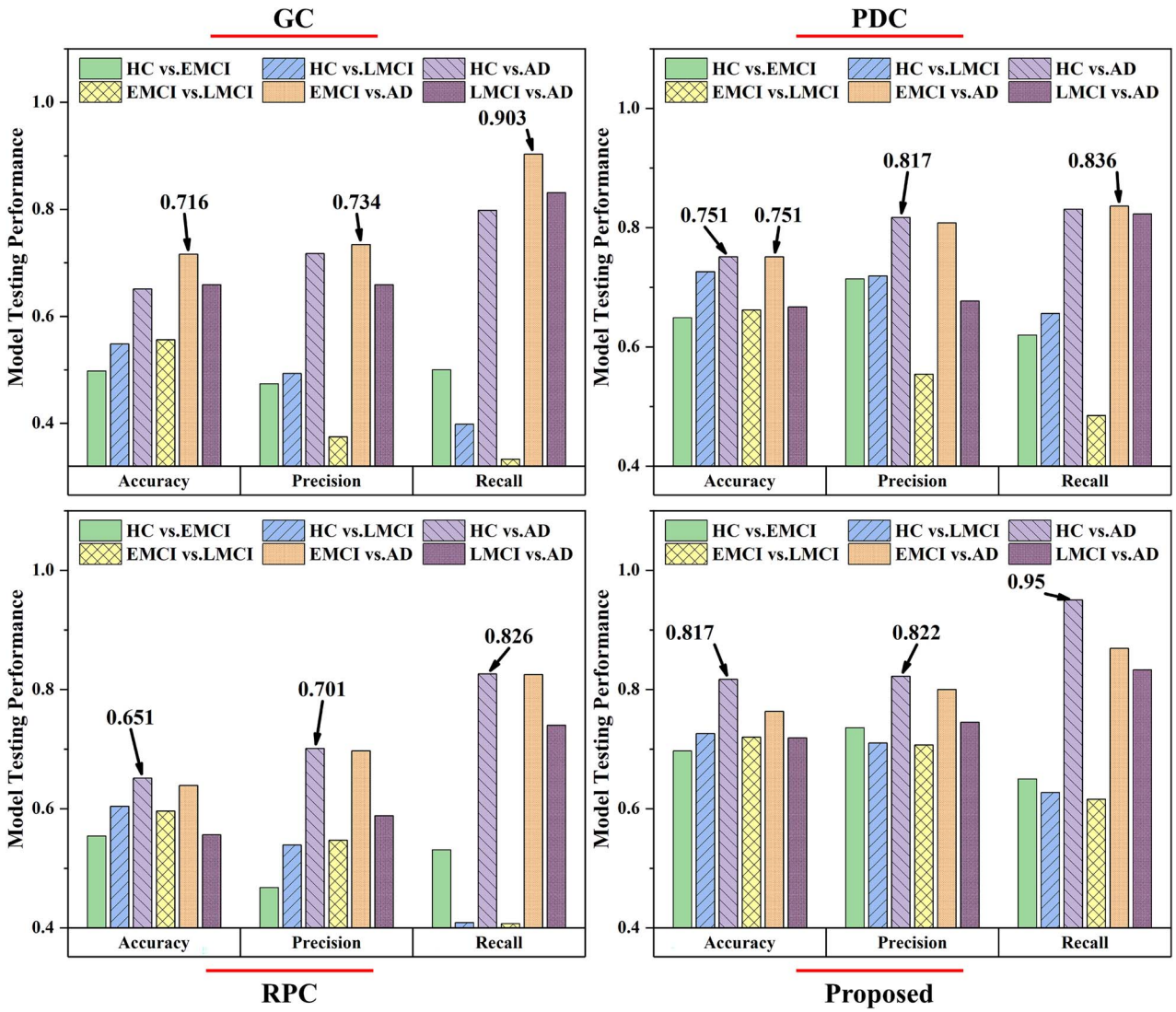

Fig. 14. Model testing results.

Table 6. Distribution of significantly different brain regions and *P*-values for HC vs. EMCI.

Area	*P*-value	Area	*P*-value	Area	*P*-value
L-4	0.003	L_3b	0.005	L_FEF	0.003
L_PEF	0.012	L_55b	0.034	L_MT	0.045
L_1	0.003	L_2	0.026	L_3a	0.000
L_6mp	0.015	L_10r	0.001	L_8Av	0.012
L_8BL	0.024	L_8C	0.004	L_IFJa	0.004
L_IFJp	0.003	L_6a	0.015	L_STGa	0.018
L_STSda	0.018	L_PH	0.011	L_TPOJ2	0.012
L_PGs	0.027	L_V6A	0.031	L_V4t	0.031
L_TE1m	0.010	R_V1	0.024	R_PEF	0.021
R_POS2	0.007	R_V3B	0.000	R_PIT	0.049
R_7Am	0.024	R_3a	0.031	R_a47r	0.005
R_a10p	0.004	R_OP1	0.001	R_RI	0.014
R_Pir	0.002	R_AAIC	0.027	R_FOP1	0.016
R_AIP	0.012	R_STGa	0.022	R_TE1a	0.005
R_TF	0.006	R_V4t	0.040	R_pOFC	0.048
R_p24	0.037				

cerebral cortex, 25 brain regions, and in the right cerebral cortex, 19 brain regions exhibited *P*-values below the significance level of 0.05. Notably, eight brain regions, namely, the 47l, 47s, 7Pm, Pol2, V1, STSda, TE1m, and pOFC regions defined by the HCP MM, showed significant differences in both the left and right cerebral cortex between the AD and HC groups.

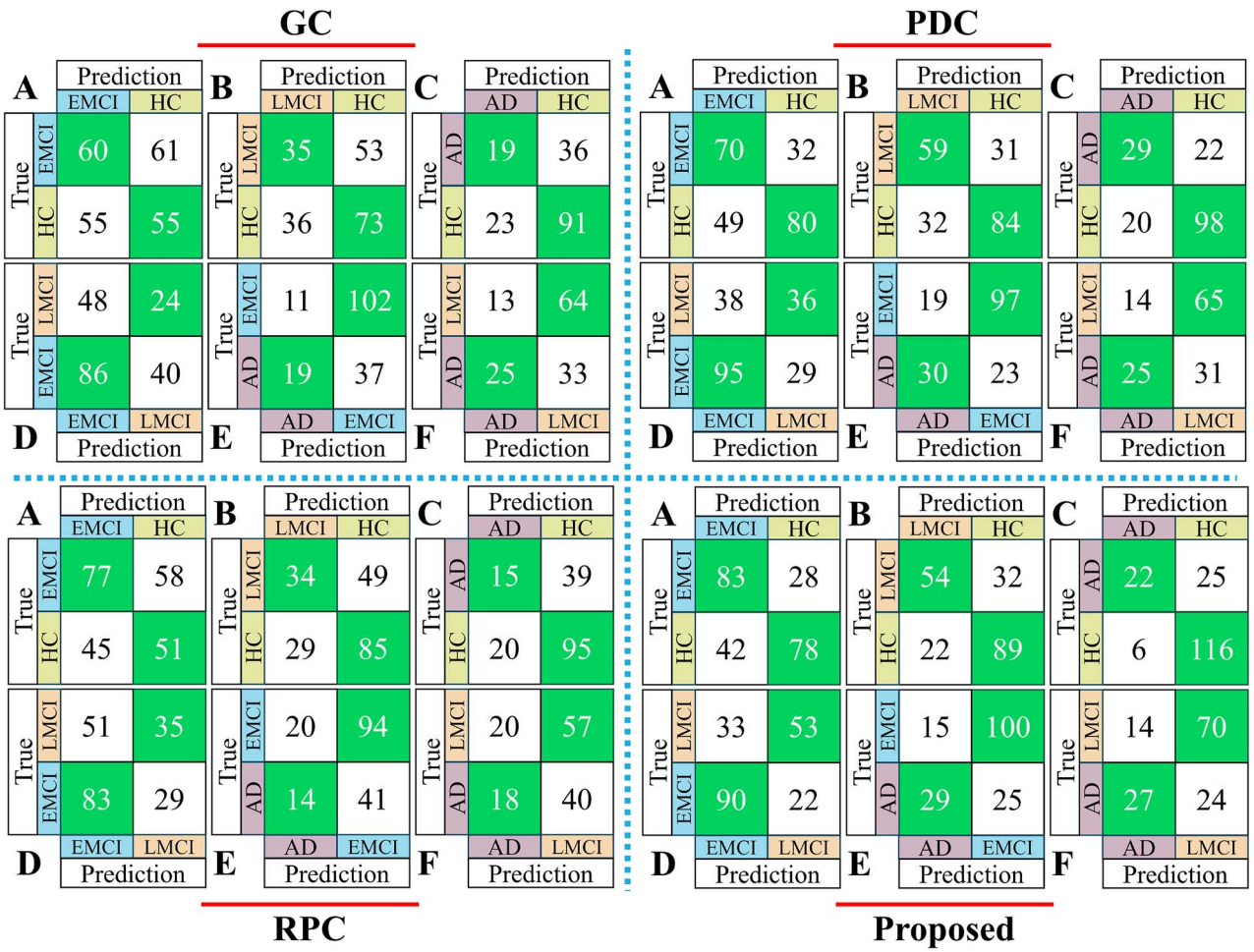

Fig. 15. Confusion matrix.

Table 7. Distribution of significantly different brain regions and *P*-values for HC vs. LMCI.

Area	*P*-value	Area	*P*-value	Area	*P*-value
L_V1	0.020	L_MST	0.002	L_4	0.029
L_V3B	0.011	L_MT	0.045	L_3a	0.001
L_8Av	0.03	L_8BL	0.004	L_9p	0.007
L_44	0.012	L_45	0.001	L_47l	0.017
L_IFJa	0.009	L_IFSp	0.003	L_p946v	0.013
L_OFC	0.014	L_AAIC	0.002	L_STSda	0.016
L_TPOJ2	0.012	L_IP0	0.003	L_TGv	0.007
R_V1	0.023	R_POS2	0.007	R_V3B	0.000
R_1	0.011	R_3a	0.031	R_47m	0.029
R_45	0.011	R_OFC	0.007	R_AIP	0.001
R_V4t	0.040				

Table 9 presents the results of the significance difference tests for PC values between the EMCI group and the LMCI group. The table shows the distribution of significantly different brain regions and their corresponding *P*-values. In the left cerebral cortex, 10 brain regions, and in the right cerebral cortex, 11 brain regions exhibited *P*-values below the significance level of 0.05. Notably, four brain regions, namely, the TE2a, AAIC, 45, and oOFC regions defined by the HCP MMP, showed significant differences in both the left and right cerebral cortex between the EMCI and LMCI groups. These findings suggest that these brain regions may play a role in distinguishing between early and late stages of mild cognitive impairment.

Table 10 presents the results of the significance difference tests for PC values between the EMCI group and the AD group. The table shows the distribution of significantly different brain regions and their corresponding *P*-values. In the left cerebral cortex, 19 brain regions, and in the right cerebral cortex, 26 brain regions exhibited *P*-values below the significance level of 0.05. Notably, two brain regions, namely, the FOP2 and pOFC regions defined by the HCP MMP, showed significant differences in both

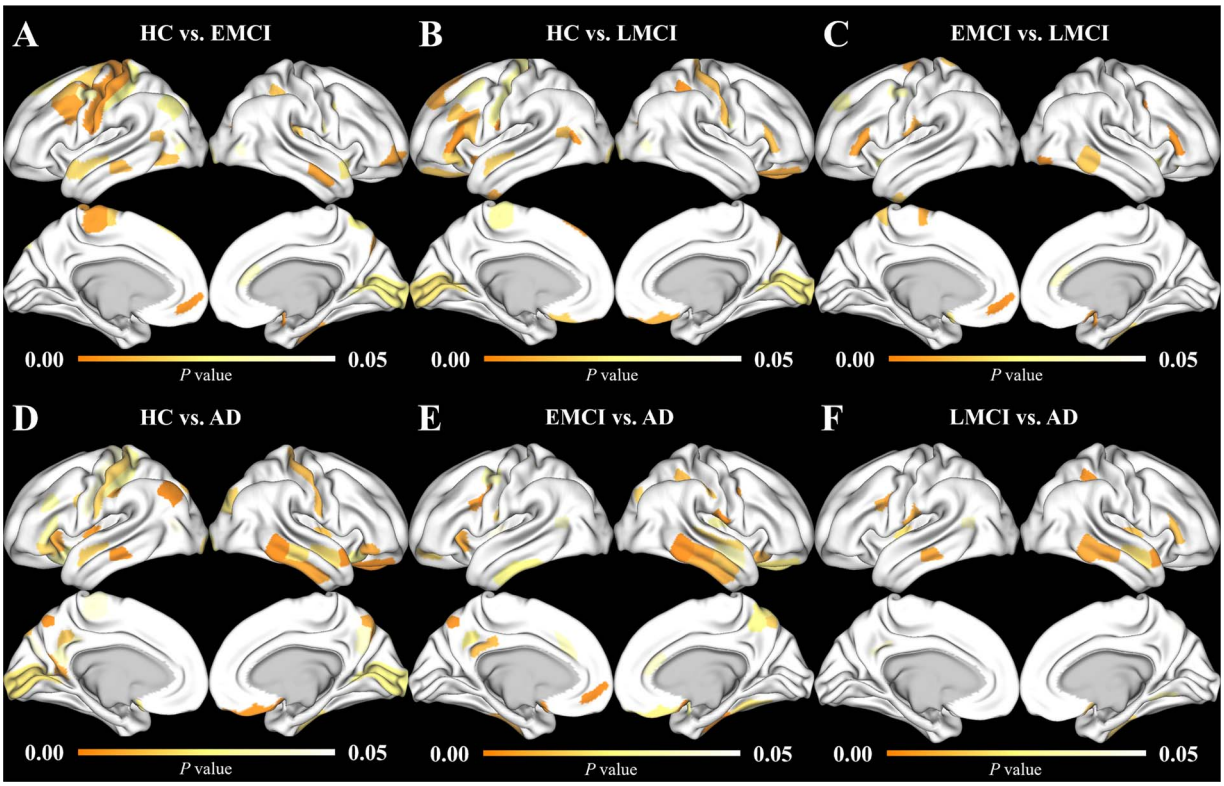

Fig. 16. Distribution of statistical differences in brain regions.

Table 8. Distribution of significantly different brain regions and *P*-values for HC vs. AD.

Area	P-value	Area	P-value	Area	P-value
L_V1	0.020	L_V6	0.043	L_4	0.041
L_MT	0.045	L_7Pm	0.001	L_POS1	0.006
L_v23ab	0.037	L_31pv	0.038	L_1	0.016
L_2	0.029	L_45	0.031	L_47l	0.017
L_IFJp	0.016	L_p946v	0.031	L_47s	0.031
L_Pol2	0.002	L_AVI	0.006	L_AAIC	0.028
L_PFt	0.007	L_STSda	0.016	L_PGs	0.000
L_V6A	0.011	L_31pd	0.014	L_pOFC	0.024
L_TE1m	0.001	R_V1	0.024	R_V3A	0.021
R_POS2	0.007	R_V7	0.016	R_V3B	0.000
R_7Pm	0.006	R_7m	0.038	R_1	0.011
R_47l	0.007	R_OFC	0.001	R_47s	0.026
R_Pol2	0.012	R_STGa	0.001	R_STSda	0.019
R_TE1p	0.000	R_TE2a	0.005	R_TF	0.020
R_pOFC	0.000	R_TE1m	0.019		

Table 9. Distribution of significantly different brain regions and *P*-values for EMCI vs. LMCI.

Area	P-value	Area	P-value	Area	P-value
L_55b	0.034	L_5L	0.015	L_6mp	0.006
L_10r	0.000	L_9p	0.032	L_45	0.004
L_OP4	0.008	L_AAIC	0.028	L_pOFC	0.021
L_TGv	0.015	R_PEF	0.000	R_PIT	0.001
R_47m	0.011	R_45	0.001	R_OP1	0.008
R_Pir	0.002	R_AAIC	0.027	R_TE1p	0.013
R_TF	0.018	R_pOFC	0.003	R_p24	0.038

Table 10. Distribution of significantly different brain regions and *P*-values for EMCI vs. AD.

Area	P-value	Area	P-value	Area	P-value
L_FEF	0.030	L_PEF	0.006	L_55b	0.034
L_7Pm	0.001	L_d23ab	0.010	L_3a	0.017
L_10r	0.000	L_IFJa	0.004	L_IFJp	0.000
L_11l	0.017	L_Pol2	0.044	L_AVI	0.006
L_FOP2	0.005	L_TE2a	0.024	L_TF	0.01
L_TPOJ2	0.038	L_31pd	0.023	L_pOFC	0.002
L_a32pr	0.036	R_PEF	0.000	R_V7	0.016
R_PIT	0.049	R_PCV	0.025	R_7Pm	0.015
R_7Am	0.023	R_OFC	0.022	R_47s	0.009
R_OP4	0.001	R_OP1	0.027	R_Pir	0.028
R_FOP2	0.031	R_PFt	0.014	R_AIP	0.010
R_A5	0.017	R_STSda	0.035	R_TE1a	0.013
R_TE1p	0.000	R_TE2a	0.008	R_TF	0.000
R_VVC	0.020	R_pOFC	0.000	R_Ig	0.031
R_STSva	0.001	R_TE1m	0.004	R_p24	0.038

Table 11. Distribution of significantly different brain regions and *P*-values for LMCI vs. AD.

Area	P-value	Area	P-value	Area	P-value
L_31pv	0.041	L_IFJa	0.008	L_IFJp	0.003
L_OP4	0.008	L_Pol2	0.019	L_TPOJ2	0.038
L_TE1m	0.005	R_7Pm	0.049	R_45	0.011
R_Pol2	0.012	R_FOP2	0.031	R_AIP	0.001
R_STGa	0.003	R_STSda	0.019	R_TE1p	0.006
R_TF	0.018	R_VMV1	0.033	R_pOFC	0.014
R_Pol1	0.003	R_STSva	0.010	R_TE1m	0.005

To visualize the results, Fig. 16 maps the brain regions and their corresponding P-values from Tables 6–11 onto a brain model. The intensity of the color in the mapping indicates the significance level, with darker colors representing smaller P-values and more pronounced differences.

the left and right cerebral cortex between the EMCI and AD groups.

Table 11 presents the results of the significance difference tests for PC values between the LMCI group and the AD group. The table shows the distribution of significantly different brain regions and their corresponding *P*-values. In the left cerebral cortex, 7 brain regions, and in the right cerebral cortex, 14 brain regions exhibited *P*-values below the significance level of 0.05. Notably, two brain regions, namely, the Pol2 and TE1m regions defined by the HCP MMP, showed significant differences in both the left and right cerebral cortex between the LMCI and AD groups.

Discussion

Contributing to revealing causal direction in complex time series models

This study initially simulated mathematical models of varying degrees of causal associations in binary and multivariate time series. It integrated the frequency domain NC research method and introduced the nCAUC metric to assess the performance of multiple methods. In the case of binary variables (scenarios 1–3), the time-domain GC method was generally able to correctly detect causal associations consistent with the mathematical models. However, in the scenario of weak associations (scenario 2), it exhibited inconsistencies with the ground truth. Both frequency domain GC and RPC methods provided erroneous results across all scenarios, while the PDC and NC methods yielded accurate conclusions. Further analysis of Fig. 7 (scenario 1, strong causality) revealed that the PDC method exhibited significant fluctuations in the computed causal values as the frequency varied along the *X*-axis. Overall, both time-domain and frequency-domain NC methods demonstrated strong discriminative capability. In the time-domain results (Fig. 7B), the causal influence of variable X on Y persisted across all lag values, with a more pronounced causal direction observed as the lag increased. In the frequency domain results (Fig. 7F), it was evident that the causal impact of variable X on Y primarily concentrated in the low-frequency region, which was consistent with the observations in Figs 9 and 10. In the defined scenario by Equation (5), the influence of past values of variable X on Y was 10 times smaller compared to the influence of Y's own past values. Such a weak causal association posed challenges for all four methods (as visualized in Fig. 8, the visual discriminative power between the two causal directions was limited). However, by considering the nCAUC metric, the causal impact of X on Y could still be accurately detected.

In the case of complex multivariate causal models, the PDC method in the cyclic causal model (scenario 4) no longer provides reliable detection results and yields incorrect conclusions regarding the relationship between time series Y and Z. Similar issues have also been raised by Khan et al. (2023), who, through synthetic and real EEG data, identified potential erroneous results in the extraction of brain effective networks using the PDC method. However, the integrated NC methods, both in the time domain and frequency domain, consistently indicate that the true causal direction is from Z to Y. In the transitivity causal model, although time series *X* does not directly influence *Z*, the integrated NC methods can still accurately perceive this relationship. By combining the information from Table 4 and Fig. 12, it is possible to infer the causal impact of *X* on *Z*. In summary, through the simulation of fMRI BOLD signals, the integration of frequency-domain NC methods contributes to revealing causal direction in complex time series models. Given the weak and indirect nature of

causal associations among brain regions, the proposed approach holds promise for significant applications in the processing of real fMRI data.

Contributing to enhancing performance of cognitive impairment prediction models at different severity levels

This study utilized directed binary causal connectivity to characterize the associations between different brain regions in a complex brain network. Additionally, the directed centrality of the 360 cortical parcels from the HCP MMP method was used as the input layer for deep learning, which was then trained. The chosen deep learning model had a simple structure and a small number of parameters, facilitating reproducibility of the results and establishing a baseline for the integrated frequency-domain NC method. Some studies (Alfakih et al. 2023; Xia et al. 2024) have designed more complex neural network structures to achieve higher classification performance. However, this study focuses on the applicability of frequency-domain causal analysis methods in AD diagnosis, thus avoiding the use of complex neural networks. In subsequent research, adjustments to the neural network's structure and optimization of parameters will indeed further enhance the model's performance.

From Fig. 13, it can be observed that all four causal analysis methods compared in this study were able to complete the training within 100 epochs, although the proposed method exhibited slower convergence and required nearly 300 iterations to converge in the HC vs. LMCI group. Nevertheless, all methods achieved training accuracy levels close to 100%. This phenomenon suggests that the models may have encountered severe overfitting issues, as mentioned in other studies (Buvaneswari and Gayathri 2023; Mujahid et al. 2023; Shamrat et al. 2023). Therefore, further analysis incorporating test performance (Table 5, Fig. 14) and confusion matrices (Fig. 15) is necessary to evaluate the performance of each method more specifically (Nancy Noella and Priyadarshini 2023; Arafa et al. 2024).

In the test results (Table 5), the integrated frequency-domain NC method demonstrated significantly superior performance in terms of accuracy, precision, and recall compared to the other three methods. Among the specific group predictions, the HC vs. AD group achieved the highest accuracy of 81.7%. This was followed by the EMCI vs. AD and HC vs. EMCI groups, while the lowest accuracy was observed in the HC vs. EMCI group, which was only 69.7%. Despite this, the accuracy was still nearly 20 percentage points higher than the binary baseline, indicating that the complex brain network topological features extracted by the integrated frequency domain NC method contribute to enhancing the performance of the deep learning model. This finding is consistent with our previous research (Wang et al. 2023). Furthermore, the high accuracy of the AD group compared to the other three groups indicates the significant characteristics of brain connectivity changes in AD patients. The lower accuracy in the HC vs. EMCI group may be attributed to less pronounced brain connectivity changes between these two groups, making it challenging to identify mild cognitive impairment at an early stage from the healthy control group (Veluppal et al. 2022; Shaji et al. 2023).

Consistent significance of brain region causal associations as potential biomarkers for AD analysis

The integrated frequency-domain NC analysis method of fMRI signals revealed consistent and significant differences in multiple newly defined brain regions within the HCP MMP cortical atlas among individuals with varying degrees of cognitive impairment. These findings can be further investigated as potential biomarkers for AD. Statistical analysis was performed to examine the NC causal values in the frequency domain between fMRI BOLD signals of different brain regions using the HCP MMP method. The names of these brain regions and their corresponding *P*-values are listed in Tables 6-11. It is evident that many brain regions exhibited significant differences across various groups. These include well-established brain regions that align with findings from previous research, such as the Primary Motor Cortex (Area 4), Primary Sensory Cortex (Area 1), Primary Visual Cortex (Area V1), and Lateral Temporal Cortex (Area TF), which are closely associated with motor, planning, perception, visual, and auditory activities (Ravikumar et al. 2021; Du et al. 2023; Yan et al. 2023; Zhang, Zhang, et al. 2023a). Additionally, several multimodal subregions were discovered for the first time using the HCP MMP method, such as Area STSd anterior (STSda) (Sheng et al. 2023), Area TE1 Middle (TE1m) (Zhao et al. 2021), Medial Area 7P (7Pm) (Kitzbichler et al. 2021), and Anterior Agranular Insula Complex (AAIC) (Sheng et al. 2021). These findings provide valuable insights into characterizing brain region variations at a finer granularity, building upon previous AD research.

Figure 17 illustrates the brain regions with significant differences that appeared in at least two pairwise comparisons and maps them onto the brain model. Among them, the pOFC (posterior orbitofrontal cortex) region exhibited the highest number of statistical differences, appearing in the right hemisphere of the HC vs. EMCI group, bilateral hemispheres of the HC vs. AD group, bilateral hemispheres of the EMCI vs. LMCI group, bilateral hemispheres of the EMCI vs. AD group, and the right hemisphere of the LMCI vs. AD group, totaling eight occurrences. This consistent significance, observed across five out of six pairwise comparisons, establishes a consistent pattern of significant differences. While no statistical differences were detected in the HC vs. LMCI group, the pOFC region exhibited statistical differences in the remaining five pairwise comparisons. Table 12 presents the distribution of brain regions with occurrence frequencies greater than or equal to four.

Limitations

This study has several limitations. Firstly, the integrated frequency-domain NC method used to analyze fMRI signals has a significantly higher computational complexity compared to other commonly used methods. Both the definition of NC values and the computation time may pose challenges for its widespread application. Similar observations have been made in the field of deep learning, where the convergence speed of frequency-domain NC is relatively slower compared to other research methods. Causality values computed proportionally range from 0 to 1, leading to larger result variances and stronger fluctuations, as observed in Figs 7–12. Consequently, this may affect the convergence speed of deep learning, especially when utilizing the Adam optimization method, which adjusts the learning rate using estimates of first and second moments. Differential computations in the 0–1 proportional results could be challenging, with a risk of gradient vanishing. Therefore, in future studies, we will also consider exploring other deep learning parameter optimization methods to improve model convergence speed.

Secondly, the integrated frequency-domain NC method has only been experimented with in binary classification problems. Currently, there is no well-defined solution for generalizing this method to multi-class scenarios (Mehmood et al. 2020) to meet

Table 12. Overview of brain regions with consistent significant differences (four or more occurrences, $P < 0.05$).

Area	HC vs. EMCI		HC vs. LMCI		HC vs. AD		EMCI vs. LMCI		EMCI vs. AD		LMCI vs. AD		Occurred times
	Left	Right	Left	Right	Left	Right	Left	Right	Left	Right	Left	Right	
pOFC		0.048			0.024	0.000	0.021	0.003	0.002	0.000		0.014	8
45			0.001	0.011	0.031		0.004	0.001				0.011	6
STSda	0.018		0.016		0.016	0.019				0.001		0.019	6
TE1m	0.010				0.001	0.019				0.004	0.005	0.005	6
TF		0.006				0.020		0.018	0.010	0.000		0.018	6
3a	0.000	0.031	0.001	0.031					0.017				5
7Pm					0.001	0.006			0.001	0.015		0.049	5
AAIC		0.027	0.002		0.028		0.028	0.027					5
PEF	0.012	0.021						0.000	0.006	0.000			5
Pol2					0.002	0.012			0.044		0.019	0.012	5
V1		0.024	0.020	0.023	0.02	0.024							5
1	0.003			0.011	0.016	0.011							4
AIP		0.012		0.001						0.010		0.001	4
IFJa	0.004		0.009						0.004		0.008		4
IFJp	0.003				0.016				0.000		0.003		4
OFC			0.014	0.007		0.001				0.022			4
STGa	0.018	0.022				0.001						0.003	4
TE1p						0.000		0.013		0.000		0.006	4
TPOJ2	0.012		0.012						0.038		0.038		4
V3B		0.000	0.011	0.000		0.000							4

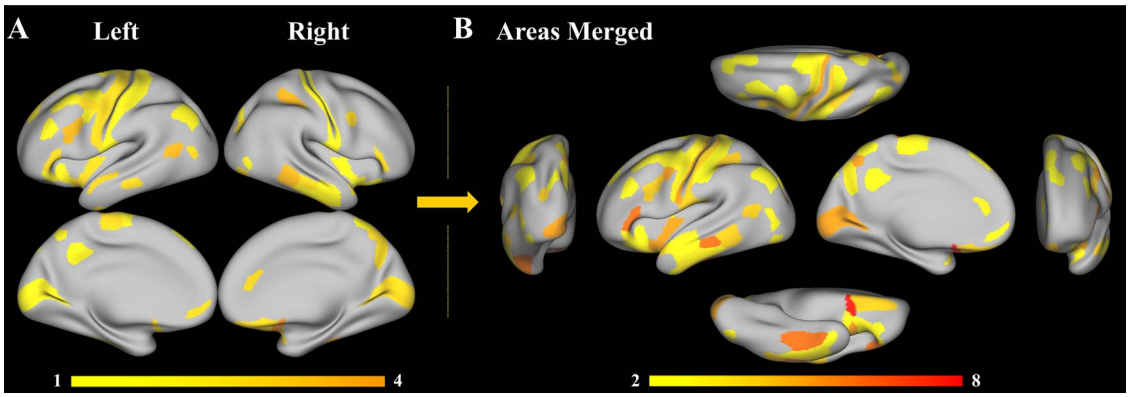

Fig. 17. Consistent significant differences in brain regions.

the requirements of higher classification prediction. Even for binary classification, the classification accuracy obtained in this study is numerically lower compared to other similar studies (Hussain et al. 2020; Tufail et al. 2020; Prajapati et al. 2021). Previous research using correlation matrix methods for calculating undirected binary or weighted complex brain networks (Sheng et al. 2019, 2021, 2022) achieved classification accuracies of over 90%. However, these studies had a very limited sample size of only around 100. The better classification performance, apart from the accuracy of the feature engineering measure itself, is more likely due to severe overfitting caused by the limited sample size. This can be observed in Fig. 13, where even though the training accuracy reaches 100%, the model's actual performance is subpar. Therefore, it is crucial to collect a larger dataset of individuals with cognitive impairment to enrich the model training, validation, and testing processes. This is a key aspect of leveraging artificial intelligence technologies in cognitive impairment identification research (An et al. 2020).

Conclusion

In conclusion, the frequency-domain NC method presented in this research demonstrates its effectiveness in constructing directed efficiency networks, providing valuable insights into the complex relationships between brain regions and cognitive function. Through simulations of different degrees of causal associations and statistical analyses of brain networks in individuals with varying degrees of cognitive impairment, the effectiveness of the frequency-domain NC method has been demonstrated. Comparative analyses with three commonly used frequency-domain causality analysis methods, GC, RPC, and PDC, have revealed limitations in their detection capabilities. GC and RPC methods often yielded results that deviated from the ground truth, while the PDC method was inadequate for capturing cyclic causality, possibly a prevalent form of connectivity in the brain. Furthermore, the outcomes of deep learning tests consistently showcased the superior performance of the frequency-domain NC method. Its classification metrics surpassed those of the other methods, emphasizing its efficacy in accurately characterizing brain connectivity patterns. Moreover, leveraging the multimodal brain parcellation method HCP MMP, significant and consistent differences were observed. These findings highlight the substantial association between fine-grained cortical subregions obtained through multimodal data segmentation and human cognitive function. These subregions hold promise as potential biomarkers for further investigation into AD.

Acknowledgments

Data collection and sharing for this project was funded by the Alzheimer's Disease Neuroimaging Initiative (ADNI) National Institutes of Health Grant U01 AG024904, USA and DOD ADNI (Department of Defense award number W81XWH-12-2-0012). ADNI is funded by the National Institute on Aging, the National Institute of Biomedical Imaging and Bioengineering, Alzheimer's Association, etc.

Author contributions

Bocheng Wang (Conceptualization, Formal analysis, Funding acquisition, Methodology, Software, Visualization, Writing—original draft).

Funding

This work is supported by the National Natural Science Foundation of China (No. 62306268).

Conflict of interest statement: None declared.

Data availability

All data are available on request. The preprocessing platform is available (http://dbcp.cuz.edu.cn), which allows great freedom in usage.

References

Ahmadi H, Fatemizadeh E, Motie-Nasrabadi A. Identifying brain functional connectivity alterations during different stages of Alzheimer's disease. *Int J Neurosci*. 2022:132(10):1005–1013. https://doi.org/10.1080/00207454.2020.1860037.

Alfakih A, Xia Z, Ali B, Mamoon S, Lu J. Deep causality variational autoencoder network for identifying the potential biomarkers of brain disorders. *IEEE Trans Neural Syst Rehabil Eng*. 2023:32:112–121. https://doi.org/10.1109/TNSRE.2023.3344995.

An N, Ding H, Yang J, Au R, Ang TF. Deep ensemble learning for Alzheimer's disease classification. *J Biomed Inform*. 2020:105:103411. https://doi.org/10.1016/j.jbi.2020.103411.

Arafa DA, Moustafa HE-D, Ali HA, Ali-Eldin AM, Saraya SF. A deep learning framework for early diagnosis of Alzheimer's disease on MRI images. *Multimed Tools Appl*. 2024:83(2):3767–3799. https://doi.org/10.1007/s11042-023-15738-7.

Barnett L, Barrett AB, Seth AK. Solved problems for granger causality in neuroscience: a response to Stokes and Purdon.

NeuroImage. 2018:178:744–748. https://doi.org/10.1016/j.neuroimage.2018.05.067.

Berron D, Vogel JW, Insel PS, Pereira JB, Xie L, Wisse LE, Yushkevich PA, Palmqvist S, Mattsson-Carlgren N, Stomrud E, et al. Early stages of tau pathology and its associations with functional connectivity, atrophy and memory. *Brain*. 2021:144(9):2771–2783. https://doi.org/10.1093/brain/awab114.

Buvaneswari P, Gayathri R. Detection and classification of Alzheimer's disease from cognitive impairment with resting-state fMRI. *Neural Comput Applic*. 2023:35(31):22797–22812. https://doi.org/10.1007/s00521-021-06436-2.

Cao J, Yang L, Sarrigiannis PG, Blackburn D, Zhao Y. Dementia classification using a graph neural network on imaging of effective brain connectivity. *Comput Biol Med*. 2024:168:107701. https://doi.org/10.1016/j.compbiomed.2023.107701.

Corona-Long CA, Chang E, Speck CL, Gallagher M, Bakker A. Atrophy of Brodmann area 36 differentiates age-related subjective memory decline from cognitively normal older adults and is associated with NPTX2. *Alzheimers Dement*. 2023:19(S24):e083059. https://doi.org/10.1002/alz.083059.

Dickie EW, Anticevic A, Smith DE, et al. Ciftify: A framework for surface-based analysis of legacy MR acquisitions. *Neuroimage*. 2019:197:818–826. https://doi.org/10.1016/j.neuroimage.2019.04.078.

Du J, Li A, Shi D, Chen X, Wang Q, Liu Z, Sun K, Guo T, Initiative ADN. Association of APOE-ε4, osteoarthritis, β-amyloid, and tau accumulation in primary motor and somatosensory regions in Alzheimer disease. *Neurology*. 2023:101(1):e40–e49. https://doi.org/10.1212/WNL.0000000000207369.

Esteban O, Markiewicz CJ, Blair RW, Moodie CA, Isik AI, Erramuzpe A, Kent JD, Goncalves M, DuPre E, Snyder M, et al. fMRIPrep: a robust preprocessing pipeline for functional MRI. *Nat Methods*. 2019:16(1):111–116. https://doi.org/10.1038/s41592-018-0235-4.

Franciotti R, Nardini D, Russo M, Onofrj M, Sensi SL, Initiative ADN, others. Comparison of machine learning-based approaches to predict the conversion to Alzheimer's disease from mild cognitive impairment. *Neuroscience*. 2023:514:143–152. https://doi.org/10.1016/j.neuroscience.2023.01.029.

Glasser MF, Sotiropoulos SN, Wilson JA, Coalson TS, Fischl B, Andersson JL, Xu J, Jbabdi S, Webster M, Polimeni JR. The minimal preprocessing pipelines for the human connectome project. *NeuroImage*. 2013:80:105–124. https://doi.org/10.1016/j.neuroimage.2013.04.127.

Glasser MF, Coalson TS, Robinson EC, Hacker CD, Harwell J, Yacoub E, Ugurbil K, Andersson J, Beckmann CF, Jenkinson M. A multi-modal parcellation of human cerebral cortex. *Nature*. 2016:536(7615):171–178. https://doi.org/10.1038/nature18933.

Hajamohideen F, Shaffi N, Mahmud M, Subramanian K, Al Sariri A, Vimbi V, Abdesselam A, Initiative ADN. Four-way classification of Alzheimer's disease using deep Siamese convolutional neural network with triplet-loss function. *Brain Inform*. 2023:10(1):5. https://doi.org/10.1186/s40708-023-00184-w.

Harrison JR, Bhatia S, Tan ZX, Mirza-Davies A, Benkert H, Tax CM, Jones DK. Imaging Alzheimer's genetic risk using diffusion MRI: a systematic review. *NeuroImage Clin*. 2020:27:102359. https://doi.org/10.1016/j.nicl.2020.102359.

Hrybouski S, Das SR, Xie L, Wisse LE, Kelley M, Lane J, Sherin M, DiCalogero M, Nasrallah I, Detre J, et al. Aging and Alzheimer's disease have dissociable effects on local and regional medial temporal lobe connectivity. *Brain Commun*. 2023:5(5):fcad245. https://doi.org/10.1093/braincomms/fcad245.

Hu S, Dai G, Worrell GA, Dai Q, Liang H. Causality analysis of neural connectivity: critical examination of existing methods and advances of new methods. *IEEE Trans Neural Netw*. 2011:22(6):829–844. https://doi.org/10.1109/TNN.2011.2123917.

Hu S, Cao Y, Zhang J, Kong W, Yang K, Zhang Y, Li X. More discussions for granger causality and new causality measures. *Cogn Neurodyn*. 2012:6(1):33–42. https://doi.org/10.1007/s11571-011-9175-8.

Hussain E, Hasan M, Hassan SZ, Azmi TH, Rahman MA, Parvez MZ. Deep learning based binary classification for alzheimer's disease detection using brain mri images. In: Zhengguo Li, Jing Zhou, Geir Grasmo, editors. *2020 15th IEEE conference on industrial electronics and applications (ICIEA)*. Kristiansand, Norway: IEEE; 2020. pp. 1115–1120. https://doi.org/10.1109/ICIEA48937.2020.9248213.

Jitsuishi T, Yamaguchi A. Searching for optimal machine learning model to classify mild cognitive impairment (MCI) subtypes using multimodal MRI data. *Sci Rep*. 2022:12(1):4284. https://doi.org/10.1038/s41598-022-08231-y.

Khan DM, Yahya N, Kamel N, Faye I. A novel method for efficient estimation of brain effective connectivity in EEG. *Comput Methods Prog Biomed*. 2023:228:107242. https://doi.org/10.1016/j.cmpb.2022.107242.

Kitzbichler MG, Aruldass AR, Barker GJ, Wood TC, Dowell NG, Hurley SA, McLean J, Correia M, Clarke C, Pointon L, et al. Peripheral inflammation is associated with micro-structural and functional connectivity changes in depression-related brain networks. *Mol Psychiatry*. 2021:26(12):7346–7354. https://doi.org/10.1038/s41380-021-01272-1.

Lanctôt KL, Boada M, Tariot PN, Dabbous F, Hahn-Pedersen J, Udayachalerm S, Raket LL, Saiontz-Martinez C, Michalak W, Weidner W, et al. Association between clinical dementia rating and clinical outcomes in Alzheimer's disease. *Alzheimers Dement Diagn Assess Dis Monit*. 2024:16(1):e12522. https://doi.org/10.1002/dad2.12522.

Matsui T, Yamashita K. Static and dynamic functional connectivity alterations in Alzheimer's disease and neuropsychiatric diseases. *Brain Connect*. 2023:13(5):307–314. https://doi.org/10.1089/brain.2022.0044.

Mehmood A, Maqsood M, Bashir M, Shuyuan Y. A deep Siamese convolution neural network for multi-class classification of Alzheimer disease. *Brain Sci*. 2020:10(2):84. https://doi.org/10.3390/brainsci10020084.

Mohammadian F, Noroozian M, Sadeghi AZ, Malekian V, Saffar A, Talebi M, Hashemi H, Mobarak Salari H, Samadi F, Sodaei F, et al. Effective connectivity evaluation of resting-state brain networks in Alzheimer's disease, amnestic mild cognitive impairment, and normal aging: an exploratory study. *Brain Sci*. 2023:13(2):265. https://doi.org/10.3390/brainsci13020265.

Mujahid M, Rehman A, Alam T, Alamri FS, Fati SM, Saba T. An efficient ensemble approach for Alzheimer's disease detection using an adaptive synthetic technique and deep learning. *Diagnostics*. 2023:13(15):2489. https://doi.org/10.3390/diagnostics13152489.

Mulyadi AW, Jung W, Oh K, Yoon JS, Lee KH, Suk H-I. Estimating explainable Alzheimer's disease likelihood map via clinically-guided prototype learning. *NeuroImage*. 2023:273:120073. https://doi.org/10.1016/j.neuroimage.2023.120073.

Nancy Noella R, Priyadarshini J. Machine learning algorithms for the diagnosis of Alzheimer and Parkinson disease. *J Med Eng Technol*. 2023:47(1):35–43. https://doi.org/10.1080/03091902.2022.2097326.

Planche V, Manjon JV, Mansencal B, Lanuza E, Tourdias T, Catheline G, Coupé P. Structural progression of Alzheimer's disease over decades: the MRI staging scheme. *Brain Commun*. 2022:4(3):fcac109. https://doi.org/10.1093/braincomms/fcac109.

Prajapati R, Khatri U, Kwon GR. An efficient deep neural network binary classifier for Alzheimer's disease classification. In: Yeong Min Jang, Takeo Fujii, editors. *2021 international conference on artificial intelligence in information and communication (ICAIIC)*. Jeju Island, Korea (South): IEEE; 2021. pp. 231–234. https://doi.org/10.1109/ICAIIC51459.2021.9415212.

Ravikumar S, Wisse L, Lim S, Irwin D, Ittyerah R, Xie L, Das SR, Lee E, Tisdall MD, Prabhakaran K, et al. Unfolding the medial temporal lobe cortex to characterize neurodegeneration due to Alzheimer's disease pathology using ex vivo imaging. In: Ahmed Abdulkadir, Seyed Mostafa Kia, Mohamad Habes, Vinod Kumar, Jane Maryam Rondina, Chantal Tax, Thomas Wolfers, editors. *Machine learning in clinical neuroimaging: 4th international workshop, MLCN 2021, held in conjunction with MICCAI 2021, Strasbourg, France, 2021 September 27, proceedings 4*. Strasbourg, France: Springer; 2021. pp. 3–12. https://doi.org/10.1007/978-3-030-87586-2_1.

Roebroeck A, Formisano E, Goebel R. Mapping directed influence over the brain using Granger causality and fMRI. *NeuroImage*. 2005:25(1):230–242. https://doi.org/10.1016/j.neuroimage.2004.11.017.

Rubinov M, Sporns O. Complex network measures of brain connectivity: uses and interpretations. *NeuroImage*. 2010:52(3):1059–1069. https://doi.org/10.1016/j.neuroimage.2009.10.003.

Schrouff J, Monteiro JM, Portugal L, Rosa MJ, Phillips C, Mourão-Miranda J. Embedding anatomical or functional knowledge in whole-brain multiple kernel learning models. *Neuroinformatics*. 2018:16(1):117–143. https://doi.org/10.1007/s12021-017-9347-8.

Shaji S, Palanisamy R, Swaminathan R. Structural irregularities in MR corpus callosal images and their association with cerebrospinal fluid biomarkers in mild cognitive impairments. *Neurosci Lett*. 2023:810:137329. https://doi.org/10.1016/j.neulet.2023.137329.

Shamrat FJM, Akter S, Azam S, Karim A, Ghosh P, Tasnim Z, Hasib KM, De Boer F, Ahmed K. AlzheimerNet: An effective deep learning based proposition for alzheimer's disease stages classification from functional brain changes in magnetic resonance images. *IEEE Access*. 2023:11:16376–16395. https://doi.org/10.1109/ACCESS.2023.3244952.

Sheng J, Wang B, Zhang Q, Liu Q, Ma Y, Liu W, Shao M, Chen B. A novel joint HCPMMP method for automatically classifying Alzheimer's and different stage MCI patients. *Behav Brain Res*. 2019:365:210–221. https://doi.org/10.1016/j.bbr.2019.03.004.

Sheng J, Wang B, Zhang Q, Zhou R, Wang L, Xin Y. Identifying and characterizing different stages toward Alzheimer's disease using ordered core features and machine learning. *Heliyon*. 2021:7:e07287. https://doi.org/10.1016/j.heliyon.2021.e07287.

Sheng J, Wang B, Zhang Q, Yu M. Connectivity and variability of related cognitive subregions lead to different stages of progression toward Alzheimer's disease. *Heliyon*. 2022:8(1):e08827. https://doi.org/10.1016/j.heliyon.2022.e08827.

Sheng J, Huang H, Zhang Q, Li Z, Zhu H, Wang J, Ying Z, Zeng J. Identification of mild cognitive impairment conversion using augmented resting-state functional connectivity under multimodal parcellation. *IEEE Access*. 2023:12:4255–4264. https://doi.org/10.1109/ACCESS.2023.3342921.

Stevenson-Hoare J, Heslegrave A, Leonenko G, Fathalla D, Bellou E, Luckcuck L, Marshall R, Sims R, Morgan BP, Hardy J, et al. Plasma biomarkers and genetics in the diagnosis and prediction of Alzheimer's disease. *Brain*. 2023:146(2):690–699. https://doi.org/10.1093/brain/awac128.

Stokes PA, Purdon PL. A study of problems encountered in granger causality analysis from a neuroscience perspective. *Proc Natl Acad Sci*. 2017:114(34):E7063–E7072. https://doi.org/10.1073/pnas.1704663114.

Tufail AB, Ma Y-K, Zhang Q-N. Binary classification of Alzheimer's disease using sMRI imaging modality and deep learning. *J Digit Imaging*. 2020:33(5):1073–1090. https://doi.org/10.1007/s10278-019-00265-5.

van der Haar D, Moustafa A, Warren SL, Alashwal H, van Zyl T. An Alzheimer's disease category progression sub-grouping analysis using manifold learning on ADNI. *Sci Rep*. 2023:13(1):10483. https://doi.org/10.1038/s41598-023-37569-0.

Veluppal A, Sadhukhan D, Gopinath V, Swaminathan R. Differentiation of Alzheimer conditions in brain MR images using bidimensional multiscale entropy-based texture analysis of lateral ventricles. *Biomed Signal Process Control*. 2022:78:103974. https://doi.org/10.1016/j.bspc.2022.103974.

Wang B, Li L, Peng L, Jiang Z, Dai K, Xie Q, Cao Y, Yu D, Initiative ADN, others. Multigroup recognition of dementia patients with dynamic brain connectivity under multimodal cortex parcellation. *Biomed Signal Process Control*. 2022:76:103725. https://doi.org/10.1016/j.bspc.2022.103725.

Wang B, Initiative ADN, others. Enhanced brain efficiency network by integrating the new causality with fMRI and its application for Alzheimer's disease study. *Biomed Signal Process Control*. 2023:86:105364. https://doi.org/10.1016/j.bspc.2023.105364.

Xia Z, Zhou T, Mamoon S, Lu J. Inferring brain causal and temporal-lag networks for recognizing abnormal patterns of dementia. *Med Image Anal*. 2024:94:103133. https://doi.org/10.1016/j.media.2024.103133.

Xue J, Yao R, Cui X, Wang B, Wei J, Wu X, Sun J, Yang Y, Xiang J, Liu Y. Abnormal information interaction in multilayer directed network based on cross-frequency integration of mild cognitive impairment and Alzheimer's disease. *Cereb Cortex*. 2023:33(8):4230–4247. https://doi.org/10.1093/cercor/bhac339.

Yan S, Yang X, Yang H, Sun Z. Decreased coherence in the model of the dorsal visual pathway associated with Alzheimer's disease. *Sci Rep*. 2023:13(1):3495. https://doi.org/10.1038/s41598-023-30535-w.

Zhang NK, Zhang SK, Zhang LI, Tao HW, Zhang G-W. Sensory processing deficits and related cortical pathological changes in Alzheimer's disease. *Front Aging Neurosci*. 2023a:15:1–15. https://doi.org/10.3389/fnagi.2023.1213379.

Zhang S, Zhao H, Wang W, Wang Z, Luo X, Hramov A, Kurths J. Edge-centric effective connection network based on muti-modal MRI for the diagnosis of Alzheimer's disease. *Neurocomputing*. 2023b:552:126512. https://doi.org/10.1016/j.neucom.2023.126512.

Zhao B, Li T, Smith SM, Fan Z, Yang X, Yang Y, Shu J, Xiong D, Wang X, Yang Y, et al. Genetic influences on the intrinsic and extrinsic functional organizations of the cerebral cortex. 2021: medRxiv. 2021–07. https://doi.org/10.1101/2021.07.27.21261187.